



# Compensation between Wnt-driven tumorigenesis and cellular responses to ribosome biogenesis inhibition in the murine intestinal epithelium

Aurélien Raveux, Aline Stedman, Sabrina Coqueran, Sandrine Vandormael-Pournin, Nick Owens, Béatrice Romagnolo, Michel Cohen-Tannoudji

## ► To cite this version:

Aurélien Raveux, Aline Stedman, Sabrina Coqueran, Sandrine Vandormael-Pournin, Nick Owens, et al.. Compensation between Wnt-driven tumorigenesis and cellular responses to ribosome biogenesis inhibition in the murine intestinal epithelium. *Cell Death and Differentiation*, 2020, 27: 2872-2887, 10.1038/s41418-020-0548-6 . pasteur-02872067

HAL Id: pasteur-02872067

<https://pasteur.hal.science/pasteur-02872067>

Submitted on 17 Jun 2020

**HAL** is a multi-disciplinary open access archive for the deposit and dissemination of scientific research documents, whether they are published or not. The documents may come from teaching and research institutions in France or abroad, or from public or private research centers.

L'archive ouverte pluridisciplinaire **HAL**, est destinée au dépôt et à la diffusion de documents scientifiques de niveau recherche, publiés ou non, émanant des établissements d'enseignement et de recherche français ou étrangers, des laboratoires publics ou privés.

1   **Compensation between Wnt-driven tumorigenesis and cellular responses to**  
2   **ribosome biogenesis inhibition in the murine intestinal epithelium**

3   Aurélien Raveux<sup>1, 2, †</sup>, Aline Stedman<sup>1, 3, †</sup>, Sabrina Coqueran<sup>1</sup>, Sandrine Vandormael-Pournin<sup>1</sup>,  
4   Nick Owens<sup>4</sup>, Béatrice Romagnolo<sup>5, 6, 7</sup> and Michel Cohen-Tannoudji<sup>1 #</sup>

5  
6   <sup>1</sup> : Early Mammalian Development and Stem Cell Biology, Institut Pasteur, CNRS UMR 3738,  
7   25 rue du Dr. Roux, F-75015, Paris, France.

8   <sup>2</sup> : Sorbonne Université, Collège Doctoral, F-75005 Paris, France

9   <sup>3</sup> : present address : Sorbonne Université, CNRS UMR7622, Inserm U1156, Institut de Biologie  
10   Paris Seine - Laboratoire de Biologie du Développement, 9 Quai Saint Bernard, F-75005 Paris,  
11   France.

12   <sup>4</sup> : Epigenetics of Stem Cells, Department of Developmental and Stem Cell Biology, Institut  
13   Pasteur, CNRS UMR3738, 25 rue du Docteur Roux, F-75015 Paris, France

14   <sup>5</sup> : Inserm, U1016, Institut Cochin, Paris, France

15   <sup>6</sup> : CNRS, UMR8104, Paris, France

16   <sup>7</sup> : Université Paris Descartes, Sorbonne Paris Cité, France

17   † : These authors contributed equally to the work

18   # Corresponding author and lead contact: Michel Cohen-Tannoudji, Early Mammalian  
19   Development and Stem Cell Biology, Institut Pasteur, CNRS UMR 3738, 25 rue du Dr. Roux,  
20   F-75015, Paris, France; E-mail: m-cohen@pasteur.fr; Phone: 33 1 45 68 84 86; Fax: 33 1 45  
21   68 86 34; website: <https://research.pasteur.fr/en/team/group-michel-cohen-tannoudji/>.

22  
23   **Running title:** Ribosome biogenesis defects and tumor initiation

24   **Keywords :** Ribosome biogenesis; Wnt signaling; Colorectal cancer; p53.

25

26     **Abstract**

27         Ribosome biogenesis inhibition causes cell cycle arrest and apoptosis through the  
28         activation of tumor suppressor-dependent surveillance pathways. These responses are  
29         exacerbated in cancer cells, suggesting that targeting ribosome synthesis may be beneficial to  
30         patients. Here, we characterize the effect of the loss-of-function of *Notchless* (*Nle*), an essential  
31         actor of ribosome biogenesis, on the intestinal epithelium undergoing tumor initiation due to  
32         acute *Apc* loss-of-function. We show that ribosome biogenesis dysfunction strongly alleviates  
33         Wnt-driven tumor initiation by restoring cell cycle exit and differentiation in *Apc*-deficient  
34         progenitors. Conversely Wnt hyperactivation attenuates the cellular responses to surveillance  
35         pathways activation induced by ribosome biogenesis dysfunction, as proliferation was  
36         maintained at control-like levels in the stem cells and progenitors of double mutants. Thus, our  
37         data indicate that, while ribosome biogenesis inhibition efficiently reduces cancer cell  
38         proliferation in the intestinal epithelium, enhanced resistance of *Apc*-deficient stem and  
39         progenitor cells to ribosome biogenesis defects may be an important concern when using a  
40         therapeutic strategy targeting ribosome production for the treatment of Wnt-dependent  
41         tumorigenesis.

42

43 INTRODUCTION

44

45 Ribosome biogenesis inhibition has emerged as a promising therapeutic strategy  
46 against cancer. Indeed, in addition to targeting the production of the ribosomes required  
47 for the increased protein synthesis demand of cancer cells<sup>1</sup>, RNA Pol I inhibition or  
48 deficiencies in ribosome biogenesis factors were shown to trigger the binding of a 5S  
49 rRNA/RPL11/RPL5 inhibitory complex to MDM2, thereby preventing p53 degradation<sup>2-</sup>  
50 <sup>4</sup>. In absence of functional p53 pathway, ribosome biogenesis dysfunction also triggers  
51 p53-independent mechanisms<sup>5</sup>. Taking advantage of specific RNA Pol I inhibitors, several  
52 *in vitro* and xenograft studies have shown that lymphoma<sup>6</sup>, melanoma, osteosarcoma,  
53 breast, colon<sup>7</sup> and lung<sup>8</sup> cancer cells display a strong and specific sensitivity to ribosome  
54 biogenesis inhibition, that induces potent p53-dependent or independent stress  
55 responses, which are not observed in normal cells<sup>6,7</sup>. As a therapeutic strategy, targeting  
56 the translational apparatus of cancer cells has two major advantages. Firstly, it is non-  
57 genotoxic and therefore minimizes the risk of inducing novel mutations in the  
58 surrounding cells. Secondly, this approach displayed so far a clear differential effect  
59 between normal cells and the tested cancer cell lines, making it theoretically possible to  
60 establish a dosage that reduces deleterious side effects while still being efficient. However,  
61 the impact of ribosome biogenesis alterations on tissues undergoing tumorigenesis *in vivo*  
62 has insufficiently been assessed until now.

63 In humans, APC is mutated in the vast majority of colorectal cancers<sup>9</sup>. In the mouse,  
64 the acute inactivation of *Apc* in the epithelium of the small intestine results in constitutive  
65 activation of the Wnt/β-catenin pathway, leading to an abnormal expansion of the  
66 proliferative compartment at the expense of differentiated cells, reminiscent of early  
67 events of adenoma formation<sup>10,11</sup>. It has been shown that *Myc* deletion largely rescues the  
68 *Apc* loss-of-function phenotype through downstream shutdown of the Wnt pathway<sup>12</sup>,  
69 suggesting that Wnt-driven tumor initiation is also *Myc*-driven. Interestingly, the  
70 aforementioned Pol I inhibitors were demonstrated to be particularly efficient on *Myc*-  
71 driven cancer cells<sup>6,8</sup>. Since c-MYC is a major ribosome biogenesis positive regulator<sup>13</sup>,  
72 this raised the possibility that ribosome biogenesis inhibition could also attenuate the  
73 phenotype caused by *Apc* deficiency.

74 *Notchless (Nle)* encodes a WD40 repeats-containing protein highly conserved in  
75 eukaryotes<sup>14-16</sup> and involved in the late steps of maturation and subsequent export of the

76 60S particle<sup>17-20</sup>. In previous studies, we showed that the role of *Nle* in the maturation of  
77 the large ribosomal subunit is conserved in the mouse<sup>21</sup>, and that *Nle* loss-of-function  
78 leads to p53 activation in the intestinal epithelium, resulting in rapid stem cell and  
79 progenitor exhaustion through cell cycle arrest, apoptosis and premature goblet cell  
80 differentiation<sup>22</sup>. This genetic model offers a unique opportunity to study the impact of  
81 ribosome biogenesis perturbations specifically in the intestinal epithelium under  
82 pathological conditions. Here, by combining *Nle* and *Apc* conditional loss-of-function, we  
83 show that defective ribosome biogenesis strongly attenuates Wnt hyperactivation-driven  
84 proliferative compartment expansion in the intestinal epithelium through restoration of  
85 cell cycle exit and differentiation. Conversely, we show that Wnt hyperactivation  
86 alleviates the *Nle* loss-of-function phenotype, as proliferation is maintained in double  
87 mutant crypts and in the stem cell compartment despite broad and persistent p53  
88 stabilization.

89

90 **MATERIAL AND METHODS**

91

92 **Mice.**

93 All experiments were conducted at the Institut Pasteur according to the French and  
94 European regulations on care and protection of laboratory animals (EC Directive 86/609,  
95 French Law 2001-486 issued on June 6, 2001) and were approved by the Institut Pasteur  
96 ethics committee (n° 2016-0106 and 2017-0044).

97 The alleles used were as follows: *Nle*<sup>flox</sup> <sup>21</sup>, *Nle*<sup>null</sup> <sup>15</sup>, *Apc*<sup>flox</sup> <sup>10</sup>, Villin-CreERT2 <sup>23</sup>. All  
98 experimental animals were generated in a mixed C57BL/6Nx129/Sv genetic background.  
99 Mice at 5 to 10 weeks of age were injected intraperitoneally with 56mg/kg tamoxifen for  
100 three consecutive days. For proliferation assays, mice were injected with BrdU (100  
101 mg/kg) 2h, 24h or 48h before sacrifice. Injection order was randomized between animals  
102 and genotype was only assessed after the experiments.

103 Genotyping was performed by PCR after tissue lysis in 50 mM Tris, pH 8.5, 100 mM NaCl,  
104 0.5% Tween 20, and 100 mg/ml proteinase K at 56°C overnight, followed by a 10-min  
105 incubation at 96°C. PCR was performed using 1.0 unit of Taq DNA polymerase (MP  
106 biomedicals) under the following conditions: 95 °C for 30 s; 32 cycles at 95 °C for 30 s,  
107 60 °C for 30 s, 72 °C for 60 s; 72 °C for 10 min. For *Nle*, PCR amplification with primers  
108 mNleQF3 (5'- ctgtactcttctatccgaccac -3'), CondF (5'- agacttgggtctggactca -3'), and  
109 CondR2 (5'- ccctaactaagacaaccaaga -3') allowed us to discriminate *Nle*<sup>wt</sup> (100 bp), *Nle*<sup>Flox</sup>  
110 (200 bp), and *Nle*<sup>del</sup> (500 bp) alleles. For *Apc*, PCR amplification with primers APCint13F  
111 (5'- ctgttctgcagtatgttatca -3'), APCext14R (5'- ctatgagtcaacacaggatta -3'), and APCext15R  
112 (5'- caataataatgagctctgggcc -3') allowed us to discriminate *APC*<sup>wt</sup> (180 bp), *Apc*<sup>Flox</sup> (230 bp),  
113 and *Apc*<sup>del</sup> (160 bp) alleles. PCR products were separated by electrophoresis on 2% high-  
114 resolution (NuSieve 3:1 agarose) agarose gels.

115

116 **Tissue extracts.**

117 For paraffin sections, the intestinal tract was dissected, then flushed with ice-cold PBS to  
118 remove feces and perfused with ice-cold 4% paraformaldehyde (PFA). The small intestine  
119 was rolled up from the proximal to the distal end in concentric circles, fixed in 4% PFA at  
120 4°C overnight and embedded in paraffin wax. For RT-qPCR on total epithelium, 5 cm of  
121 duodenum was harvested in 10mL EDTA (10mM in PBS, pH=8.0). After 30 min incubation  
122 on ice and 2x5 min vortex at maximum speed at 4°C, the muscle layer of the intestine was

123 manually removed and the epithelium was pelleted at 300 rcf, 4°C for 5 min, then  
124 resuspended in 1 mL Trizol (Invitrogen, Carlsbad, CA, USA). For crypts and villi isolation,  
125 5–10 cm of jejunum were collected, opened longitudinally and processed as previously  
126 described<sup>24</sup>.

127

128 **Histology and immunostaining.**

129 Histology and immunostaining were performed as described previously<sup>25</sup>. Specific  
130 antibody binding was detected using biotinylated secondary antibodies and  
131 Streptavidin/HRP complexes (Dako, Glostrup, Denmark). For β-catenin immunostaining,  
132 M.O.M. and ABC kits (Vector) were used. Bright field microscopy was performed using a  
133 Axio Scan.Z1 equipped with a 20x objective lens. The system was set to run in automated  
134 batch mode with automated focus and tissue finding. Primary and secondary antibodies  
135 used in this study are listed in Supplementary material Supplementary Table S1.

136

137 **In situ hybridization.**

138 For Fluorescent In Situ Hybridization (FISH), the hybridization step was performed as  
139 previously described. Conjugated FISH probes were purchased from Eurogentec: its1-  
140 Cy5: tagacacggaagagccggacggaaaga; its2-Cy3: gcgattgatcgtcaaccgacgctc and validated in  
141 a previous study<sup>21</sup>. ISH for Olfm4 was carried out with the RNAscope 2.5 BROWN kit  
142 (Advanced Cell Diagnostics) according to the manufacturer's instructions (Olfm4 probe  
143 reference: 311831).

144

145 **RT-qPCR.**

146 RNA extraction was performed according to the Trizol-chloroform extraction protocol  
147 provided by Invitrogen. For epithelium, crypts and villi, the chloroform and ethanol steps  
148 were repeated twice. Reverse-transcription was performed using the Superscript II kit  
149 (Invitrogen) according to the manufacturers' instructions. Real-time PCR was carried on  
150 using custom-designed primers (Supplementary Table S2) and LightCycler 480 SYBR  
151 Green I Master mix (Roche Life Sciences) on a LightCycler 480 (Roche Life Sciences).  
152 Expression levels were normalized using TBP and Aldolase as reference genes.

153

154 **Western blot.**

155 Proteins were extracted in a buffer containing 10mM Tris-HCl pH 7.5, 5mM EDTA, 150mM  
156 NaCl, 30mM Sodium Pyrophosphate, 50mM Sodium Fluoride, 10% Glycerol, 1% NP40,  
157 supplemented with antiproteases (Roche Life Sciences) and 2.5U/ $\mu$ L Benzonase (Sigma-  
158 Aldrich). The extracts were incubated on ice for 30 min, then centrifuged 10 min at 10000  
159 rcf, 4°C. The supernatant was recovered and its protein content was determined using a  
160 Bradford assay. Proteins were denatured in Laemmli buffer at 95 °C for 5 min before being  
161 loaded on a 12% polyacrylamide gel. After migration, proteins were transferred onto a  
162 nitrocellulose membrane (Biorad, Hercules, CA, USA) and incubated overnight at 4°C with  
163 the primary antibodies. Membranes were incubated with peroxidase-labeled secondary  
164 antibodies at RT for 80 min and rinsed in TBS-0.1% Tween. Signals were visualized using  
165 ECL 2 (Pierce Biotechnology, Rockford, IL, USA) and quantified on a Typhoon Instrument.  
166 Primary and secondary antibodies used in these experiments are listed in Supplementary  
167 Table S1.

168

#### 169 **Quantification of protein synthesis.**

170 Mice were injected intraperitoneally with 2mg of puromycin in PBS, 10min before  
171 sacrifice. Intestines were rapidly harvested in ice-cold PBS containing emetine to block  
172 further puromycin incorporation during the procedure. Crypts were isolated as  
173 previously described <sup>24</sup> and counted before being lysed in protein extraction buffer.  
174 Puromycilated peptide chains were quantified on a western blot against puromycin by  
175 measuring the pixel intensity through the whole length of each lane using a Typhoon  
176 instrument.

177

#### 178 **Crypts culture.**

179 Isolated crypts were cultured as previously described <sup>45</sup>. In brief, crypts were embedded  
180 in growth factor reduced matrigel (Corning LifeSciences, Tewksbury, MA, USA) with  
181 culture medium (Advanced DMEM/F12; Invitrogen) containing EGF (Peprotech, Rocky  
182 Hill, NJ, USA), R-spondin 1 (R&D Systems, Minneapolis, MN, USA), Noggin (Peprotech) and  
183 B27 (Invitrogen). For nutlin-3 treatment, 4- or 8-days old organoids derived from Control  
184 or APC<sup>cKO</sup> crypts were incubated with culture medium containing DMSO (mock condition)  
185 or nutlin-3a (Sigma) at 1 $\mu$ M, 5 $\mu$ M and 10 $\mu$ M concentrations. After 2 days of treatment, the  
186 number of healthy organoids was scored manually. Images of representative organoids  
187 were acquired with a bright-field Leica MZ16 binocular (Leica, M165FC). Healthy

188 organoids were defined as budding structures with at least 3 buds and visible lumen for  
189 Control, and smooth spheres with visible lumen for APC<sup>cKO</sup>. 2 mice per genotype and 2 to  
190 3 technical replicates per condition were assessed. For immunofluorescence, organoids  
191 were fixed in 4% formaldehyde for 2 hours at RT, permeabilized with Blocking Buffer (5%  
192 fetal calf serum, 0.5% Triton X-100 in 1X PBS) and incubated with appropriate primary  
193 and secondary antibodies. Phalloidin (1/50; ThermoFisher) and DAPI (1/1000; Sigma)  
194 were used to detect cell membranes and nuclei, respectively. Samples were washed 3  
195 times in PBS before being imaged on the macroapoptome Zeiss Axiozoomer and analyzed  
196 using the Zen software.

197

198 **Statistical analysis.** All experiments were performed with a sample size n≥4 (each  
199 sample is an individual mouse) so as to dampen the influence of outliers on means. No  
200 animal was excluded from the analysis. For mean comparisons, all bar graphs with pooled  
201 data show means ± S.E.M. Statistical analyses were performed using the parametric  
202 Student's t-test and the non-parametric Mann-Whitney Wilcoxon test to account for the  
203 possibility of non-normal distributions. p<0.05 was considered significant. Tests were  
204 always two-sided.

205

206 **RNA sequencing.** Crypts were harvested at day 1 and day 2 pi from 3 mice of each  
207 genotypes and total RNA was prepared using Trizol-chloroform extraction. PolyA-  
208 enriched library preparation and PE150 sequencing were performed by Novogene Co. Ltd.  
209 Approximately 20 million sequences were generated per sample and used for the analysis.  
210 The sequence data have been deposited in NCBI's Gene Expression Omnibus under  
211 accession number GSE144233.

212

### 213 **Computational Methods**

#### 214 *RNA-seq Data Processing and Differential Expression*

215 Paired end RNA-seq reads were quantified against the mm9 transcriptome using Kallisto  
216 0.43<sup>26</sup> with default options. Rounded estimated counts were used as input to DESeq2<sup>27</sup>.  
217 Genes with at least 10 normalized counts in all replicates of at least one condition were  
218 considered for differential expression analysis. For all differential expression tests  
219 DESeq2 was run without independent filtering and without any fold change shrinkage,  
220 genes with padj < 0.05 are considered differentially expressed. Samples at 24h and 48h

were processed separately and subjected to the same analysis. We performed Wald tests under the model  $\sim \text{Nle} + \text{Apc} + \text{Nle:Apc}$ , where Nle is a factor indicating  $\text{Nle}^{\text{cKO}}$  and Apc is a factor indicating  $\text{Apc}^{\text{cKO}}$ . Roughly, for each gene, the fold changes in  $\text{Nle}^{\text{cKO}}$  samples (N) and in  $\text{Apc}^{\text{cKO}}$  samples (A) were calculated. The interaction term (D) indicates that, for a given gene, the fold change in  $\text{Apc}^{\text{cKO}};\text{Nle}^{\text{cKO}}$  samples differs from  $\text{N} * \text{A}$ . We tested the significance of the Nle, Apc and the interaction term.

*K-means clustering of RNA-seq Data*

Response patterns of genes were identified using k-means clustering (using the Clustering package in Julia 0.6<sup>28</sup>) on normalised read counts. We clustered the mean expression per timepoint and condition, normalised to the maximum expression of each gene. We found  $k = 10$  provided a balance, both generalising broad behaviours and identify specific double cKO results.

*Gene/phenotype ontology enrichment analysis*

Genes were annotated with gene ontology (GO) terms (transitively closed to include parent terms) from the MGI GO annotation (date : 26/01/2017). Enrichment tests were applied to gene lists resulting from differential expression analysis. In all cases, enrichment tests were performed using  $\chi^2$  tests for all terms with at least 5 genes in the gene list of interest against a background of annotations of all genes tested for differential expression.  $\chi^2$  test p-values were adjusted by the Benjamini-Hochberg method, those with  $\text{padj} < 0.05$  where reported.

The different gene clusters from the model-based analysis were also analyzed using the MouseMine database. For each gene list, Mammalian Phenotype Ontology Enrichment terms were searched with Max p-value = 0.05 and Holm-Bonferroni correction. When significantly enriched terms were found, those relevant to our mutant phenotypes were selected, and the term with the lowest p-value for each category was indicated on figures 5E and S5. For every analysis,  $p < 0.05$  is considered significant.

247

248 **RESULTS**

249

250 **Nle loss-of-function improves survival of *Apc*-deficient mice and limits expansion of**  
251 **the crypt compartment.**

252 Control (Villin-CreERT2<sup>tg/0</sup>; *Apc*<sup>flox/+</sup>; *Nle*<sup>flox/+</sup>), *Apc*<sup>cKO</sup> (Villin-CreERT2<sup>tg/0</sup>;  
253 *Apc*<sup>flox/flox</sup>; *Nle*<sup>flox/+</sup>) and *Apc*<sup>cKO</sup>; *Nle*<sup>cKO</sup> (Villin-CreERT2<sup>tg/0</sup>; *Apc*<sup>flox/flox</sup>; *Nle*<sup>flox/null</sup>) mice were  
254 subjected to three daily intraperitoneal tamoxifen injections and analyzed at various time  
255 points post last tamoxifen injection (pi) (Figure 1A). Conversion of the *Apc*<sup>flox</sup> and *Nle*<sup>flox</sup>  
256 alleles into *Apc*<sup>del</sup> and *Nle*<sup>del</sup> alleles respectively, was monitored by genomic PCR on both  
257 loci. We found that recombination of the *Apc*<sup>flox</sup> and *Nle*<sup>flox</sup> alleles was efficient in the  
258 intestinal epithelium from Control, *Apc*<sup>cKO</sup> and *Apc*<sup>cKO</sup>; *Nle*<sup>cKO</sup> mice (Figure 1B). *Apc*<sup>cKO</sup>  
259 mice lost weight and died rapidly following tamoxifen injection. Weight loss was  
260 significantly reduced in double mutant mice (Figure 1C), and although persisting, their  
261 death was significantly delayed compared to the *Apc*<sup>cKO</sup> (Figure 1D).

262 Consistent with previous reports<sup>10,11</sup>, hematoxylin-eosin staining showed that *Apc*  
263 loss-of-function resulted in rapid expansion of the crypt compartment at the expense of  
264 the villus (Figure 1E), loss of typical enterocyte polarity and abnormal nuclear  
265 morphology (Figure S1A). *Nle* loss-of-function strongly dampened these histological  
266 alterations (Figure 1E), as the enlarged crypt compartment was not observed, and cell  
267 polarity was restored in the villus (Figure S1A). Other aspects of the *Apc* loss-of-function  
268 phenotype such as the ectopic paneth cells<sup>10</sup> and enterocyte hypertrophy were similarly  
269 observed in *Apc*<sup>cKO</sup>; *Nle*<sup>cKO</sup> (Figure S1A-C). Collectively, these data indicate that *Nle* loss-  
270 of-function restores crypt and villus architecture in the *Apc*-deficient epithelium but does  
271 not fully rescue the *Apc* loss-of-function clinical and histological phenotype.

272

273 ***Nle* loss-of-function attenuates proliferative compartment expansion by restoring**  
274 **cell cycle exit and differentiation despite Wnt pathway hyperactivation.**

275 To verify that Wnt hyperactivation was effective in *Apc*<sup>cKO</sup>; *Nle*<sup>cKO</sup> intestinal epithelia,  
276 we monitored nuclear β-catenin on small intestine sections. Accumulation of nuclear β-  
277 catenin was similarly observed in *Apc*<sup>cKO</sup> and *Apc*<sup>cKO</sup>; *Nle*<sup>cKO</sup> intestines (Figure 2A).  
278 Moreover, upregulation of the Wnt targets *c-Myc* and *Axin2* was found in both *Apc*<sup>cKO</sup> and  
279 *Apc*<sup>cKO</sup>; *Nle*<sup>cKO</sup> epithelia (Figure 2B), confirming that hyperactivation of the Wnt/β-catenin  
280 pathway consecutive to *Apc*-deficiency was not modified by *Nle* loss-of-function.

We then performed a 2hrs BrdU chase to visualize proliferation in the intestinal epithelium at day 2, 3 and 4 pi (Figure 2C and S2A). As previously reported<sup>10,11</sup>, proliferation in *Apc*<sup>cKO</sup> intestines abnormally extended beyond the histological crypt compartment. Strikingly, the proliferation pattern was restored in *Apc*<sup>cKO</sup>; *Nle*<sup>cKO</sup>, as BrdU positive cells restricted to the histological crypt like in Control intestines (Figure 2C). The proportion of BrdU-positive cells within the proliferative compartment was similar for all genotypes (Figure 2D), suggesting that the structure of the cell cycle is not dramatically perturbed in *Apc*<sup>cKO</sup> and *Apc*<sup>cKO</sup>; *Nle*<sup>cKO</sup> compared to Control. We observed a linear growth of their proliferative compartment overtime (Figure S2B-C), primarily due to enlarged crypt growth in *Apc*<sup>cKO</sup>, whereas in *Apc*<sup>cKO</sup>; *Nle*<sup>cKO</sup>, it was caused by histological crypt hyperplasia (Figure S2A). Taken together, these data suggest that *Nle* loss-of-function reduces the expansion of the proliferative compartment consecutive to *Apc* loss-of-function without affecting the proliferation rate of *Apc*-deficient intestinal progenitors.

We next tested whether such attenuation could be due to a restoration of cell cycle exit by comparing the position of BrdU-positive cells after short and long periods of chase at day 2 and 3 pi. After 48h of chase, while BrdU-positive cells had exited cell cycle and were found in the villus in Control, all *Apc*<sup>cKO</sup> BrdU-positive cells remained in the proliferative compartment (Figure 3A and S3A), thereby contributing to its expansion. Of note, BrdU staining was fainter in *Apc*<sup>cKO</sup> than in Control, suggesting that *Apc*<sup>cKO</sup> progenitors underwent more cell divisions than Control cells. In *Apc*<sup>cKO</sup>; *Nle*<sup>cKO</sup> intestine, BrdU-positive cells reached the villus after 48h chase at day 3pi. However, at day 2pi, BrdU-positive cells were found in the crypt and at the boundary between the crypt and the villus (Figure S3A-B) suggesting that though restored, cell-cycle exit is delayed in *Apc*<sup>cKO</sup>; *Nle*<sup>cKO</sup>. *Nle*-deficiency induced a potent apoptotic response in normal intestinal progenitors<sup>22</sup>. Caspase 3 staining on intestinal sections showed a similar proportion of Caspase-3-positive cells in both *Apc*<sup>cKO</sup> and *Apc*<sup>cKO</sup>; *Nle*<sup>cKO</sup> proliferative compartments (Figure 3B, E), indicating that apoptosis is unlikely to be an important driver for the reduction of the proliferative compartment in the *Apc*<sup>cKO</sup>; *Nle*<sup>cKO</sup>. Finally, to evaluate the differentiation status of *Apc*<sup>cKO</sup> and *Apc*<sup>cKO</sup>; *Nle*<sup>cKO</sup> epithelia, we performed Mucin-2 and Chromogranin-A immunohistochemistry (Figure 3C-D) and Alcian Blue coloration (Figure S3C). Enteroendocrine and goblet cells were absent from the expanded proliferative compartment of the *Apc*<sup>cKO</sup> as previously reported<sup>10,11</sup>. In contrast, both cell types were found in *Apc*<sup>cKO</sup>; *Nle*<sup>cKO</sup> villi and crypts. Consistently, *Muc2* and *ChromoA* mRNA

314 levels in  $Apc^{cKO}$ ;  $Nle^{cKO}$  crypts were intermediate compared to  $Apc^{cKO}$  and Controls (Figure  
315 3F). Collectively, our results indicate that *Nle* loss-of-function attenuates Wnt  
316 hyperactivation-driven expansion of the proliferation compartment by partially restoring  
317 the capacity of *Apc*-deficient progenitors to exit cell cycle and differentiate.

318

319 ***Nle* loss-of-function leads to ribosome biogenesis defects and p53 stabilization in**  
320 **the *Apc*-deficient epithelium.**

321 The immediate consequences of *Apc* loss-of-function on ribosome biogenesis and  
322 protein synthesis in intestinal epithelium have not been described so far. No difference in  
323 the levels of nucleolar rRNA intermediates of the small (its1) and the large (its2)  
324 ribosomal subunits was observed in  $Apc^{cKO}$  compared to Control crypts at day 2 pi (Figure  
325 4A-B) indicating that rRNA synthesis was not affected in *Apc*-deficient progenitors.  
326 Performing FISH with its1 and its2 probes, we previously showed increased ribosome  
327 biogenesis in crypts compared to villi<sup>22</sup>. Consistent with the invasion of proliferative cells  
328 into the villus region, FISH staining of  $Apc^{cKO}$  showed high pre-rRNAs levels in a region  
329 corresponding to the expanded proliferative compartment (Figure 4C). These data  
330 indicate that ribosome production in *Apc*-deficient proliferative cells is similar to that of  
331 *Apc*-proficient intestinal progenitors.

332 *Nle* loss-of-function was shown to affect large ribosomal subunit biogenesis in  
333 crypt cells<sup>22</sup> leading to the specific increase in its2, but not its1, levels. A similar  
334 phenotype was detected in  $Apc^{cKO}$ ;  $Nle^{cKO}$  crypts at day 2 pi (Figure 4B-C), however its2  
335 accumulation was no longer restricted to crypt cells but largely extended to villi (Figure  
336 4C). A possible explanation for this observation would be that  $Apc^{cKO}$ ;  $Nle^{cKO}$  progenitors,  
337 unlike  $Nle^{cKO}$  (Villin-CreERT2<sup>tg/0</sup>;  $Nle^{flox/null}$ ) progenitors, survived and continued to  
338 proliferate despite dysfunctional ribosome biogenesis, thereby giving rise to  
339 differentiated cells with increased nucleolar ribosomal pre-particles.

340 We next asked whether these defects activated a p53 stress response, as in a  
341 normal epithelium<sup>22</sup>. In  $Apc^{cKO}$ , p53 was transiently stabilized at day 2 pi in a few cells  
342 located at the distalmost part of the expanded proliferative compartment (Figure 4D and  
343 S4A) consistent with previous reports<sup>29</sup>. In  $Apc^{cKO}$ ;  $Nle^{cKO}$ , strong and persistent p53  
344 nuclear staining was observed in most cells of the crypt and of the lower part of the villus  
345 (Figure 4D and S4B), like its2 accumulation (Figure 4C). Importantly, robust p53  
346 stabilization was observed in  $Apc^{cKO}$ ;  $Nle^{cKO}$  progenitors in absence of cell cycle arrest

347 (Figures 2A and S2) or massive apoptotic response (Figure 3B) contrary to *Nle*<sup>cKO</sup> crypt  
348 cells<sup>22</sup>. Collectively, our data show that *Nle* loss-of-function leads to defective ribosome  
349 biogenesis and p53 stabilization in *Apc*-deficient progenitor cells without triggering the  
350 cell cycle arrest and apoptotic responses normally observed in *Apc*-proficient cells.

351

352 **The double mutant transcriptome is essentially the sum of single mutant  
353 transcriptomes.**

354 We performed RNAseq on Control, *Nle*<sup>cKO</sup>, *Apc*<sup>cKO</sup> and *Apc*<sup>cKO</sup>; *Nle*<sup>cKO</sup> crypts at day  
355 1 and 2 pi (Figure 5; Supplementary Table S3). Principal component analysis clearly  
356 distinguished samples according to their genotype (Figure 5A), with PC1 (58.79% of the  
357 variance) and PC2 (12.77% of the variance) segregating the samples according to the *Apc*  
358 or *Nle* genotype respectively. *Apc*<sup>cKO</sup>; *Nle*<sup>cKO</sup> samples were undistinguishable from *Apc*<sup>cKO</sup>  
359 according to PC1 and from *Nle*<sup>cKO</sup> according to PC2, indicating that *Apc*<sup>cKO</sup>; *Nle*<sup>cKO</sup> is  
360 essentially the linear combination of *Nle*<sup>cKO</sup> and *Apc*<sup>cKO</sup>. Using K-means clustering, we  
361 found that the 15115 genes expressed in our dataset could be spread into 10 clusters with  
362 distinct gene expression variation patterns (Figure 5B; Supplementary Table S4).  
363 Strikingly, the vast majority of the genes had the same expression pattern in *Apc*<sup>cKO</sup>; *Nle*<sup>cKO</sup>  
364 as in *Apc*<sup>cKO</sup>, with only four clusters (6, 7, 9 and 10) comprising 3259 (21%) genes that  
365 were differentially regulated in *Apc*<sup>cKO</sup>; *Nle*<sup>cKO</sup> compared to *Apc*<sup>cKO</sup> samples. Gene  
366 expression pattern varied little according to the timing.

367 To distinguish additive from non-additive interactions between the two mutations,  
368 we performed a model-based analysis where timings were considered separately (Figure  
369 5C-D). Considering all samples at a given time point, a “*Nle*-related”, an “*Apc*-related” fold-  
370 change and an interaction term describing the deviation of the double mutant from a  
371 linear combination of the two mutants were calculated for each gene. Examining cases  
372 where the effects of the double mutant were either an independent combination of both,  
373 or exhibited a dependence, we distinguished 8 gene categories (Figure 5C; Supplementary  
374 Table S5), four of which encompassed genes that were subject to non-additive  
375 interactions (*ie* have a “D” term). Consistent with the principal component analysis, *Apc*  
376 loss-of-function was largely dominant compared to *Nle* loss-of-function (91% vs 38% of  
377 misregulated genes at day 2 pi) (Figure 5D). Besides genes that were either unaffected in  
378 all genotypes ([-|-|-]) and those affected only by *Apc* or *Nle* loss of function ([A|-|-] and [-  
379 |N|-]), a minority of genes was subject to either additive ([A|N|-], 15% of misregulated

genes at day 2 pi) or non-additive interactions ( $[-|-|D]$ ,  $[-|N|D]$ ,  $[A|-|D]$ , and  $[A|N|D]$ , 14% of misregulated genes at day 2 pi) (Figure 5D). Gene and phenotype ontology enrichment analysis (Figures 5E and S5) showed that *Apc* or *Nle* loss of function upregulated genes involved in ribosome biogenesis in an additive manner (Figure 5E,  $[A|N|-]$ ). Interestingly, the sub-cluster of genes that are expressed at intermediate levels in  $Apc^{cKO}; Nle^{cKO}$  due to the additive effect of *Apc*-related upregulation and *Nle*-related downregulation is significantly enriched in genes involved in cell cycling and proliferation (Figure 5E,  $[A|N|-]$ ). Overall, hypothesizing that the observed phenotypic differences arises from differential gene regulation at the transcriptional level, these results suggest that the phenotype of the  $Apc^{cKO}; Nle^{cKO}$  essentially results from additive gene-by-gene effects of *Apc* and *Nle* loss-of-function rather than signaling pathway transcriptional activation or shutdown.

We next examined a few sets of genes whose differential expression might be relevant to the  $Apc^{cKO}; Nle^{cKO}$  phenotype (Figure 5F). Upregulation of cell cycle inhibitor genes in  $Apc^{cKO}; Nle^{cKO}$  progenitors compared to  $Apc^{cKO}$  might explain their enhanced capacity to stop proliferating. However, *p21* was the only cell cycle inhibitor upregulated in  $Apc^{cKO}; Nle^{cKO}$  to levels similar to  $Nle^{cKO}$ . This was likely due to p53 activation since *p21* is a well-known p53 target. Other p53 targets were equally upregulated in  $Apc^{cKO}; Nle^{cKO}$  and  $Nle^{cKO}$ , including those that were downregulated in the  $Apc^{cKO}$  (*Fas*, *Perp*). Thus, Wnt hyperactivation does not dramatically impact *p53* transcriptional response. Conversely, most Wnt targets were similarly upregulated in  $Apc^{cKO}; Nle^{cKO}$  and  $Apc^{cKO}$ , suggesting that *Nle* loss-of-function only marginally modulates the Wnt hyperactivation transcriptional response. Finally, intestinal stem cell marker expression in  $Apc^{cKO}; Nle^{cKO}$  resulted from either additive (*Ascl2*, *Sox9*, *Tert*, *Pw1*, *Bmi1*) or non-additive (*Olfm4*, *Lgr5*, *Mex3a*, *Lrig1*, *Krt15*, *Hopx*) effects. Strikingly, *Nle* loss-of-function attenuated Wnt hyperactivation-driven *Lgr5* upregulation but also participated to the synergic upregulation of the reserve stem cell markers *Krt15* and, to a lesser extend *Hopx* and *Bmi1*. This suggests that the reserve intestinal stem cell population might be particularly stimulated in the  $Apc^{cKO}; Nle^{cKO}$  intestine.

***Nle* loss-of-function leads to a reduction of mature rRNAs and protein synthesis activity in *Apc*-deficient crypts.**

We next asked whether alterations in ribosome content and protein synthesis activity could contribute to the phenotype. We first quantified the levels of mature rRNAs (18S and 28S) by RT-qPCR (Figure 4A). No difference in rRNA levels was observed in *Apc*<sup>cKO</sup> crypts compared to Control at day 2 pi (Figure 6A) indicating that, like pre-rRNA, ribosome content was not affected in *Apc*-deficient progenitors. We also monitored protein synthesis by puromycin incorporation *in vivo*<sup>22</sup>. Surprisingly, quantification of puromycylated nascent chains after a short *in vivo* pulse of puromycin revealed an increased number of active ribosomes in *Apc*-deficient progenitors compared to the control at day 2 and day 3 pi (Figure 6B-C, S6). Taken together with the aforementioned analyses of pre-rRNA levels, these data indicate that upregulation of protein synthesis, but not ribosome biogenesis, is an early feature of *Apc*-deficient progenitors.

Interestingly, contrary to the *Nle*<sup>cKO</sup>, mature rRNA levels were significantly decreased in *Apc*<sup>cKO</sup>; *Nle*<sup>cKO</sup> crypts (Figure 6A). It can be hypothesized that progenitor survival and proliferation despite ribosome biogenesis defects in the *Apc*<sup>cKO</sup>; *Nle*<sup>cKO</sup> gives rise to cells with decreased ribosome content. Strikingly, the number of active ribosomes in *Apc*<sup>cKO</sup>; *Nle*<sup>cKO</sup> crypt cells reduced to normal level compared to *Apc*<sup>cKO</sup> (Figure 6B-C, S6). Altogether, these data suggest that, in the context of *Apc*-deficient intestinal epithelium, *Nle* loss-of-function leads to a reduction of ribosome content consecutive to ribosome biogenesis defects, which, in turn, decreases translational activity of *Apc*-deficient progenitors to control-like levels. Such impairment of translation stimulation might contribute to induce cell cycle exit in *Apc*<sup>cKO</sup>; *Nle*<sup>cKO</sup> progenitors.

433

#### 434 **Wnt hyperactivation prevents p53-induced rapid depletion of intestinal stem and** 435 **progenitor cells in *Nle*-deficient crypts.**

We then examined the fate of intestinal stem cells in *Apc*<sup>cKO</sup>; *Nle*<sup>cKO</sup> mice. RT-qPCR confirmed the transcriptomic data as *Lgr5* was upregulated in the *Apc*<sup>cKO</sup> and restored to control levels in the *Apc*<sup>cKO</sup>; *Nle*<sup>cKO</sup> at day 2 pi, whereas *Olfm4* was downregulated in both *Nle*<sup>cKO</sup> and *Apc*<sup>cKO</sup>; *Nle*<sup>cKO</sup> compared to Control (Figure 7A). *In situ* hybridization indicated that, as expected, *Olfm4* expression confined to cells at the crypt bottom in Control, extended upward in *Apc*<sup>cKO</sup> and was markedly decreased in *Nle*<sup>cKO</sup> (Figure 7B). In *Apc*<sup>cKO</sup>; *Nle*<sup>cKO</sup>, *Olfm4* staining was similar to *Apc*<sup>cKO</sup> but varied from crypt to crypt and was generally fainter than both Control and *Apc*<sup>cKO</sup>. Interestingly, nuclear p53 protein was detected in crypt base columnar (CBC) cells, recognizable by their shape and location at

445 the crypt base, at every tested time point (Figure 7C) suggesting that, like progenitors,  
446 *Apc*-deficient stem cells were less sensitive to ribosome biogenesis defects and p53  
447 activation than *Apc*-proficient stem cells. Indeed, contrary to *Nle*<sup>cKO</sup>, proliferating CBCs  
448 were present at the bottom of *Apc*<sup>cKO</sup>; *Nle*<sup>cKO</sup> crypts (Figure 7D). Collectively, these data  
449 show that intestinal stem and progenitor cells are maintained in *Apc*<sup>cKO</sup>; *Nle*<sup>cKO</sup> mice  
450 despite defective ribosome biogenesis and robust p53 activation.

451 To confirm this point, we derived organoids from control, *Nle*<sup>cKO</sup>, *Apc*<sup>cKO</sup> and  
452 *Apc*<sup>cKO</sup>; *Nle*<sup>cKO</sup> crypts harvested at day 1 pi (Figure 8A-B). Contrary to *Nle*<sup>cKO</sup> crypts,  
453 *Apc*<sup>cKO</sup>; *Nle*<sup>cKO</sup> crypts grew into organoids at the same rate as Control (Figure 8A). Of note,  
454 *Apc*<sup>cKO</sup>; *Nle*<sup>cKO</sup> organoids grew as spheroids like *Apc*<sup>cKO</sup> (Figure 8B). Over time,  
455 *Apc*<sup>cKO</sup>; *Nle*<sup>cKO</sup> organoids were progressively populated by *Nle*-proficient cells that had  
456 escaped recombination at the *Nle* locus. This, together with the fact that continuous Cre  
457 induction is detrimental to organoid growth<sup>46</sup>, prevented us to assess the behavior of  
458 *Apc*<sup>cKO</sup>; *Nle*<sup>cKO</sup> organoids at later time points. In order to highlight possible increased  
459 resistance to p53 activation of *Apc*<sup>cKO</sup> stem and progenitor cells compared to Control, we  
460 cultured organoids with increasing doses of nutlin-3, a small compound that activates p53  
461 through inhibition of Mdm2. *Apc*<sup>cKO</sup> organoids were more resistant to nutlin-3 treatment  
462 than Control, as viability of Control was strongly reduced at 5µM nutlin-3 while that of  
463 *APC*<sup>cKO</sup> organoids was almost unaffected (Figure 8D) despite robust p53 stabilization  
464 (Figure S7B). Collectively, these results show that *Apc*<sup>cKO</sup>; *Nle*<sup>cKO</sup> intestinal stem and  
465 progenitor cells display enhanced survival to p53 activation.

466

467 **DISCUSSION**

468

469 Colorectal cancers, like many cancers, are characterized by increased ribosome  
470 biogenesis and protein translation<sup>30,31</sup>. High expression of pre-rRNA is associated with  
471 poor prognosis in colorectal cancer<sup>32</sup> and increased translational elongation is key for  
472 intestinal tumorigenesis<sup>33</sup>. Interestingly, oxaliplatin, a drug commonly used to treat  
473 colorectal cancers, was shown to affect ribosome biogenesis and trigger p53 induction  
474 and, consistent with this, cancer cells sensitive to oxaliplatin display higher ribosome  
475 biogenesis and mRNA translation rates<sup>34</sup>. Here, we showed that *in vivo* gut epithelium-  
476 specific inhibition of ribosome biogenesis strongly attenuates the expansion of the  
477 proliferative compartment during tumor initiation.

478 Inactivation of some key target genes of the Wnt/β-catenin pathway such as *c-*  
479 *Myc*<sup>12</sup>, *cyclinD2*<sup>35</sup> and *Fak1*<sup>36</sup> or of the chromatin remodeling factor *Brg1*<sup>37</sup> were also  
480 shown to dampen the expansion of the proliferative compartment in *Apc*<sup>cKO</sup> mice. In all  
481 these situations, dampening was accompanied by a marked alteration of the Wnt  
482 hyperactivation transcriptional signature. In contrast, *Nle* loss-of-function only  
483 marginally modifies the transcriptomic response to *Apc* loss-of-function. The partial  
484 rescue of *Apc*<sup>cKO</sup>; *Nle*<sup>cKO</sup> mice phenotype is thus rather due to the compensation between  
485 the antagonistic effects of Wnt-driven tumorigenesis and ribosome biogenesis inhibition.

486 In *Apc*<sup>cKO</sup>; *Nle*<sup>cKO</sup> mice, attenuation likely results from the activation of the  
487 RP/MDM2/p53 ribosome biogenesis surveillance pathway. Upon *Apc* inactivation, p53  
488 stabilization is observed only locally and transiently in a small population of cells and the  
489 intestinal phenotype of *Apc* loss-of-function is not modified in absence of p53 (this study  
490 and <sup>29</sup>). In contrast, high levels of p53 are detected in *Apc*<sup>cKO</sup>; *Nle*<sup>cKO</sup> crypt and villus cells  
491 showing dysfunctional ribosome biogenesis, recognizable by their nucleolar  
492 accumulation of precursor rRNAs of the large ribosomal subunit. Contrary to *Apc*-  
493 deficient progenitors, *Apc*<sup>cKO</sup>; *Nle*<sup>cKO</sup> progenitors are able to exit cell cycle and  
494 differentiate. Upregulation by p53 of *p21* could be contributing to the restoration of cell  
495 cycle arrest and attenuation of the expansion of the proliferative compartment. Another  
496 explanation for this attenuation is that *Apc*<sup>cKO</sup>; *Nle*<sup>cKO</sup> progenitors are unable to upregulate  
497 protein synthesis at a level sufficient for tumorigenesis. We show here that increased  
498 protein translation is an immediate hallmark of *Apc* loss-of-function that is no longer  
499 observed in *Apc*<sup>cKO</sup>; *Nle*<sup>cKO</sup> progenitors. Enhanced translation likely increases the

500 production of important rate-limiting cell cycle regulators and could influence the  
501 capacity of cells to divide or not. Similar to *Nle* loss-of-function, genetic or pharmacologic  
502 inhibition of mTORC1-dependent translational stimulation limits the expansion of the  
503 proliferative compartment during tumor initiation<sup>33</sup>. The reduction of the translational  
504 potential of *Apc*<sup>cKO</sup>; *Nle*<sup>cKO</sup> progenitors may therefore contribute to their eventual cell  
505 cycle exit and differentiation.

506 *Apc*-deficiency dramatically modifies the cellular responses of intestinal cells to  
507 defective ribosome biogenesis. Indeed, while *Apc*<sup>cKO</sup>; *Nle*<sup>cKO</sup> stem cells and progenitors  
508 express high levels of nuclear p53 and display a clear p53 transcriptional signature, they  
509 do not elicit the strong proliferation arrest and apoptotic responses normally observed in  
510 crypt cells<sup>22</sup>. Crosstalk between the Wnt/β-catenin pathway and p53 have been  
511 previously reported and involve the direct or indirect modulation of p53 stability by  
512 GSK3<sup>38,39</sup>. However, the regulation of p53 activity by GSK3 leads to p53 degradation,  
513 suggesting that this is not the mechanism through which *Apc* loss-of-function attenuates  
514 p53 activation in *Apc*<sup>cKO</sup>; *Nle*<sup>cKO</sup> crypt cells. Rather, the fate of stem and progenitor cells  
515 with an activated RP/MDM2/p53 ribosome biogenesis surveillance pathway may be  
516 modified by the transcriptional response to Wnt/β-catenin hyperactivation, such as for  
517 example increased expression of *Ppan*, which has been previously shown to elicit anti-  
518 apoptotic activities in intestinal stem cells and progenitors<sup>40</sup>. On a different note, it has  
519 been shown that the Wnt pathway modulates protein stoichiometry of polysomal  
520 ribosomes during mouse neocortex development<sup>41</sup>, which, in turns could potentially  
521 result in significant modulation of the proteome<sup>42</sup>. If it holds true in the intestine, such  
522 qualitative changes in translation may also contribute to the different behaviors of  
523 intestinal cells to p53 activation.

524 It is unclear why intestinal progenitors eventually exit cell cycle in *Apc*<sup>cKO</sup>; *Nle*<sup>cKO</sup>  
525 mice. Disequilibrium between the antagonistic actions of Wnt hyperactivation and  
526 defective ribosome biogenesis may trigger proliferation arrest. The extended  
527 proliferative compartment of the *Apc* mutant is in many respects heterogeneous, in  
528 particular regarding p53 stabilization (this study and <sup>29</sup>) and p21 expression<sup>43</sup>, which  
529 concern a small population of cells located at the leading edge of the proliferative  
530 compartment. It is therefore possible that while leaving the crypt domain, *Apc*<sup>cKO</sup>; *Nle*<sup>cKO</sup>  
531 progenitors experience a suprainduction of p53 and p21, which, together with increased  
532 concentration of pro-differentiation cues such as BMPs, trigger cell cycle exit. At the same

533 time, *Apc*<sup>cKO</sup>; *Nle*<sup>cKO</sup> progenitors located in the crypt domain are able to proliferate despite  
534 defective ribosome biogenesis, giving rise to cells with reduced numbers of ribosomes.  
535 Such decrease may also be interpreted as a signal for proliferation arrest, as suggested by  
536 the impaired proliferation of primary human cell lines with a defective RP/MDM2/p53  
537 ribosome biogenesis surveillance pathway<sup>44</sup>.

538 Our work also unravels major modifications of the *Nle* loss-of-function phenotype  
539 by *Apc*-deficiency. Importantly, our demonstration that *Apc*-deficient stem cells and  
540 progenitors are resistant to defective ribosome biogenesis challenges the notion that  
541 cancer cells, and in particular c-MYC-driven cancer cells, are more sensitive to ribosome  
542 biogenesis inhibition than normal cells<sup>6-8</sup>. Moreover, enhanced survival of stem cells to  
543 ribosome biogenesis stress under Wnt hyperactivation conditions may be a major  
544 limitation for therapeutic strategies targeting ribosome production, not only for  
545 colorectal cancers, but also for other cancers associated with deregulation of the Wnt/β-  
546 catenin pathway such as cutaneous melanoma, breast carcinoma, hepatocarcinoma or  
547 pancreatic ductal adenocarcinoma.

548

549 **AKNOWLEDGMENTS**

550 Imaging analyses was performed at the Imagopole and the histopathology Unit of the Institut  
551 Pasteur. We are grateful to the staff of the animal facility of Institut Pasteur for animal care and  
552 their help during this work. We thank G. Comai for technical help and advices on RNAscope  
553 ISH. This work was supported by the Fondation ARC pour le Recherche sur le cancer  
554 (PGA120140200873), the Institut Pasteur, the Centre National de la Recherche Scientifique,  
555 the Agence Nationale de la Recherche (ANR-10-LABX-73-01 REVIVE) and the Institut  
556 National du Cancer (INCa 2007-1-COL-6-IC-1 and PLBIO09-070). A.R. was supported by the  
557 Université Pierre et Marie Curie and received fellowship from the French Ministère de  
558 l'Enseignement Supérieur et de la recherche, the Fondation ARC pour la Recherche sur le  
559 Cancer and the REVIVE Labex. A. S. received support from the Fondation des Treilles.

560

561 **Competing interests :** The authors declare no competing interest.

562

563

564 **REFERENCES**

565

- 566 1 Ruggero D, Pandolfi PP. Does the ribosome translate cancer? *Nat Rev Cancer* 2003; **3**:  
567 179–192.
- 568 2 Fumagalli S, Ivanenkov VV, Teng T, Thomas G. Suprainduction of p53 by disruption  
569 of 40S and 60S ribosome biogenesis leads to the activation of a novel G2/M  
570 checkpoint. *Genes & Development* 2012; **26**: 1028–1040.
- 571 3 Bursać S, Brdovčak MC, Pfannkuchen M, Orsolić I, Golomb L, Zhu Y et al. Mutual  
572 protection of ribosomal proteins L5 and L11 from degradation is essential for p53  
573 activation upon ribosomal biogenesis stress. *Proceedings of the National Academy of  
574 Sciences* 2012; **109**: 20467–20472.
- 575 4 Donati G, Peddigari S, Mercer CA, Thomas G. 5S ribosomal RNA is an essential  
576 component of a nascent ribosomal precursor complex that regulates the Hdm2-p53  
577 checkpoint. *Cell Rep* 2013; **4**: 87–98.
- 578 5 Challagundla KB, Sun X-X, Zhang X, DeVine T, Zhang Q, Sears RC et al. Ribosomal  
579 protein L11 recruits miR-24/miRISC to repress c-Myc expression in response to  
580 ribosomal stress. *Mol Cell Biol* 2011; **31**: 4007–4021.
- 581 6 Bywater MJ, Poortinga G, Sanij E, Hein N, Peck A, Cullinane C et al. Inhibition of RNA  
582 Polymerase I as a Therapeutic Strategy to Promote Cancer-Specific Activation of p53.  
583 *Cancer Cell* 2012; **22**: 51–65.
- 584 7 Peltonen K, Colis L, Liu H, Trivedi R, Moubarek MS, Moore HM et al. A targeting  
585 modality for destruction of RNA polymerase I that possesses anticancer activity.  
586 *Cancer Cell* 2014; **25**: 77–90.
- 587 8 Kim DW, Wu N, Kim Y-C, Cheng P-F, Basom R, Kim D et al. Genetic requirement for  
588 Mycl and efficacy of RNA Pol I inhibition in mouse models of small cell lung cancer.  
589 *Genes & Development* 2016; **30**: 1289–1299.
- 590 9 Brannon AR, Vakiani E, Sylvester BE, Scott SN, McDermott G, Shah RH et al.  
591 Comparative sequencing analysis reveals high genomic concordance between  
592 matched primary and metastatic colorectal cancer lesions. *Genome Biol* 2014; **15**:  
593 454.
- 594 10 Andreu P, Colnot S, Godard C, Gad S, Chafey P, Niwa-Kawakita M et al. Crypt-  
595 restricted proliferation and commitment to the Paneth cell lineage following Apc loss  
596 in the mouse intestine. *Development* 2005; **132**: 1443–1451.
- 597 11 Sansom OJ, Reed KR, Hayes AJ, Ireland H, Brinkmann H, Newton IP et al. Loss of Apc  
598 in vivo immediately perturbs Wnt signaling, differentiation, and migration. *Genes &  
599 Development* 2004; **18**: 1385–1390.
- 600 12 Sansom OJ, Meniel VS, Muncan V, Phesse TJ, Wilkins JA, Reed KR et al. Myc deletion  
601 rescues Apc deficiency in the small intestine. *Nature* 2007; **446**: 676–679.

- 602 13 van Riggelen J, Yetil A, Felsher DW. MYC as a regulator of ribosome biogenesis and  
603 protein synthesis. *Nat Rev Cancer* 2010; **10**: 301–309.
- 604 14 Royet J, Bouwmeester T, Cohen SM. Notchless encodes a novel WD40-repeat-  
605 containing protein that modulates Notch signaling activity. *Embo J* 1998; **17**: 7351–  
606 7360.
- 607 15 Cormier S, Le Bras S, Souilhol C, Vandormael-Pournin S, Durand B, Babinet C *et al.*  
608 The Murine Ortholog of Notchless, a Direct Regulator of the Notch Pathway in  
609 *Drosophila melanogaster*, Is Essential for Survival of Inner Cell Mass Cells. *Mol Cell*  
610 *Biol* 2006; **26**: 3541–3549.
- 611 16 Gazave E, Lapébie P, Richards GS, Brunet F, Ereskovsky AV, Degnan BM *et al.* Origin  
612 and evolution of the Notch signalling pathway: an overview from eukaryotic  
613 genomes. *BMC Evol Biol* 2009; **9**: 249.
- 614 17 la Cruz de J, Sanz-Martínez E, Remacha M. The essential WD-repeat protein Rsa4p is  
615 required for rRNA processing and intra-nuclear transport of 60S ribosomal subunits.  
616 *Nucleic Acids Research* 2005; **33**: 5728–5739.
- 617 18 Ulbrich C, Diepholz M, Baßler J, Kressler D, Pertschy B, Galani K *et al.*  
618 Mechanochemical Removal of Ribosome Biogenesis Factors from Nascent 60S  
619 Ribosomal Subunits. *Cell* 2009; **138**: 911–922.
- 620 19 Matsuo Y, Granneman S, Thoms M, Manikas R-G, Tollervey D, Hurt E. Coupled GTPase  
621 and remodelling ATPase activities form a checkpoint for ribosome export. *Nature*  
622 2014; **505**: 112–116.
- 623 20 Barrio-Garcia C, Thoms M, Flemming D, Kater L, Berninghausen O, Baßler J *et al.*  
624 Architecture of the Rix1-Rea1 checkpoint machinery during pre-60S-ribosome  
625 remodeling. *Nat Struct Mol Biol* 2015; **23**: 37–44.
- 626 21 Le Bouteiller M, Souilhol C, Cormier S, Stedman A, Burlen-Defranoux O, Vandormael-  
627 Pournin S *et al.* Notchless-dependent ribosome synthesis is required for the  
628 maintenance of adult hematopoietic stem cells. *Journal of Experimental Medicine*  
629 2013; **210**: 2351–2369.
- 630 22 Stedman A, Beck-Cormier S, Le Bouteiller M, Raveux A, Vandormael-Pournin S,  
631 Coqueran S *et al.* Ribosome biogenesis dysfunction leads to p53-mediated apoptosis  
632 and goblet cell differentiation of mouse intestinal stem/progenitor cells. *Cell Death*  
633 *Differ* 2015; **22**: 1865–1876.
- 634 23 Marjou El F, Janssen K-P, Chang BH-J, Li M, Hindie V, Chan L *et al.* Tissue-specific and  
635 inducible Cre-mediated recombination in the gut epithelium. *Genesis* 2004; **39**: 186–  
636 193.
- 637 24 Guo J, Longshore S, Nair R, Warner BW. Retinoblastoma protein (pRb), but not p107  
638 or p130, is required for maintenance of enterocyte quiescence and differentiation in  
639 small intestine. *J Biol Chem* 2009; **284**: 134–140.

- 640 25 Léguillier T, Vandormael-Pournin S, Artus J, Houlard M, Picard C, Bernex F *et al.*  
641 Omcg1 is critically required for mitosis in rapidly dividing mouse intestinal  
642 progenitors and embryonic stem cells. *Biol Open* 2012; **1**: 648–657.
- 643 26 Bray NL, Pimentel H, Melsted P, Pachter L. Near-optimal probabilistic RNA-seq  
644 quantification. *Nat Biotechnol* 2016; **34**: 525–527.
- 645 27 Love MI, Huber W, Anders S. Moderated estimation of fold change and dispersion for  
646 RNA-seq data with DESeq2. *Genome Biol* 2014; **15**: 550.
- 647 28 Bezanson J, Edelman A, Karpinski S, Shah VB. Julia: A Fresh Approach to Numerical  
648 Computing. *SIAM Review* 2017; **59**: 65–98.
- 649 29 Reed KR, Meniel VS, Marsh V, Cole A, Sansom OJ, Clarke AR. A limited role for p53 in  
650 modulating the immediate phenotype of Apc loss in the intestine. *BMC Cancer* 2008;  
651 **8**: 162.
- 652 30 Pelletier J, Thomas G, Volarevic S. Ribosome biogenesis in cancer: new players and  
653 therapeutic avenues. *Nat Rev Cancer* 2017; **4**: a003681.
- 654 31 Bastide A, David A. The ribosome, (slow) beating heart of cancer (stem) cell.  
655 *Oncogenesis* 2018; **7**: 34.
- 656 32 Tsoi H, Lam KC, Dong Y, Zhang X, Lee CK, Zhang J *et al.* Pre-45s rRNA promotes colon  
657 cancer and is associated with poor survival of CRC patients. *Oncogene* 2017.  
658 doi:10.1038/onc.2017.86.
- 659 33 Faller WJ, Jackson TJ, Knight JRP, Ridgway RA, Jamieson T, Karim SA *et al.* mTORC1-  
660 mediated translational elongation limits intestinal tumour initiation and growth.  
661 *Nature* 2015; **517**: 497–500.
- 662 34 Bruno PM, Liu Y, Park GY, Murai J, Koch CE, Eisen TJ *et al.* A subset of platinum-  
663 containing chemotherapeutic agents kills cells by inducing ribosome biogenesis  
664 stress. *Nature Medicine* 2017; **23**: 461–471.
- 665 35 Cole AM, Myant KB, Reed KR, Ridgway RA, Athineos D, van den Brink GR *et al.* Cyclin  
666 D2-Cyclin-Dependent Kinase 4/6 Is Required for Efficient Proliferation and  
667 Tumorigenesis following Apc Loss. *Cancer Research* 2010; **70**: 8149–8158.
- 668 36 Ashton GH, Morton JP, Myant KB, Phesse TJ, Ridgway RA, Marsh V *et al.* Focal  
669 adhesion kinase is required for intestinal regeneration and tumorigenesis  
670 downstream of Wnt/c-Myc signaling. *Dev Cell* 2010; **19**: 259–269.
- 671 37 Holik AZ, Young M, Krzystyniak J, Williams GT, Metzger D, Shorning BY *et al.* Brg1  
672 loss attenuates aberrant wnt-signalling and prevents wnt-dependent  
673 tumorigenesis in the murine small intestine. *PLoS Genet* 2014; **10**: e1004453.
- 674 38 Eom T-Y, Jope RS. GSK3 beta N-terminus binding to p53 promotes its acetylation. *Mol  
675 Cancer* 2009; **8**: 14.

- 676 39 Kulikov R, Boehme KA, Blattner C. Glycogen synthase kinase 3-dependent  
677 phosphorylation of Mdm2 regulates p53 abundance. *Mol Cell Biol* 2005; **25**: 7170–  
678 7180.
- 679 40 Pfister AS, Keil M, Kühl M. The Wnt Target Protein Peter Pan Defines a Novel p53-  
680 independent Nucleolar Stress-Response Pathway. *Journal of Biological Chemistry*  
681 2015; **290**: 10905–10918.
- 682 41 Kraushar ML, Viljetic B, Wijeratne HRS, Thompson K, Jiao X, Pike JW et al. Thalamic  
683 WNT3 Secretion Spatiotemporally Regulates the Neocortical Ribosome Signature  
684 and mRNA Translation to Specify Neocortical Cell Subtypes. *Journal of Neuroscience*  
685 2015; **35**: 10911–10926.
- 686 42 Genuth NR, Barna M. Heterogeneity and specialized functions of translation  
687 machinery: from genes to organisms. *Nat Rev Genet* 2018; **13**: 1.
- 688 43 Cole AM, Ridgway RA, Derkits SE, Parry L, Barker N, Clevers H et al. p21 loss blocks  
689 senescence following Apc loss and provokes tumourigenesis in the renal but not the  
690 intestinal epithelium. *EMBO Mol Med* 2010; **2**: 472–486.
- 691 44 Teng T, Mercer CA, Hexley P, Thomas G, Fumagalli S. Loss of tumor suppressor  
692 RPL5/RPL11 does not induce cell cycle arrest but impedes proliferation due to  
693 reduced ribosome content and translation capacity. *Mol Cell Biol* 2013; **33**: 4660–  
694 4671.
- 695 45 Sato T, Vries RG, Snippert HJ, van de Wetering M, Barker N, Stange DE et al. Single  
696 Lgr5 stem cells build crypt-villus structures in vitro without a mesenchymal niche.  
697 *Nature* 2009; **459**: 262–265.
- 698 46 Bohin N, Carlson EA, Samuelson LC. Genome Toxicity and Impaired Stem Cell  
699 Function after Conditional Activation of CreERT2 in the Intestine. *Stem Cell Reports*  
700 2018; **11**: 1337–1346.

702 **FIGURE LEGENDS**

703

704 **Figure 1 Nle loss-of-function improves survival of Apc-deficient mice and limits**  
705 **crypt hyperplasia.** (A) Scheme of tamoxifen injection and analysis. (B) Detection of the  
706 nonrecombined (flox) and the recombined (del) *Apc* (top) and *Nle* (bottom) alleles by PCR  
707 performed on DNA extracts from Control, *Apc*<sup>cKO</sup> and *Apc*<sup>cKO</sup>; *Nle*<sup>cKO</sup> small intestinal  
708 epithelium. Two bands of similar intensity are amplified from *Apc*<sup>flox/del</sup> (top) and *Nle*<sup>flox/del</sup>  
709 (bottom) DNA (T). The wt allele appears on the gel for *Apc* but not for *Nle*. (C) Weight  
710 curve of Control, *Apc*<sup>cKO</sup> and *Apc*<sup>cKO</sup>; *Nle*<sup>cKO</sup> mice following tamoxifen injection. \*, p<0.05  
711 \*\*\*, p<0.001 according to Student's t-test. (D) Kaplan-Meier survival curve of Control,  
712 *Apc*<sup>cKO</sup> and *Apc*<sup>cKO</sup>; *Nle*<sup>cKO</sup> mice following tamoxifen injection. The difference between  
713 *Apc*<sup>cKO</sup> and *Apc*<sup>cKO</sup>; *Nle*<sup>cKO</sup> is significant with p<0.05 according to Mann-Whitney Wilcoxon  
714 test. (E) Hematoxylin-eosin staining of intestinal epithelium sections from Control, *Apc*<sup>cKO</sup>  
715 and *Apc*<sup>cKO</sup>; *Nle*<sup>cKO</sup> small intestines at day 2 pi. Black bars indicate the crypt compartment  
716 (enlarged in the *Apc*<sup>cKO</sup>). Scale bars, 50 µm.

717

718 **Figure 2 Nle loss-of-function limits the expansion of the proliferative compartment**  
719 **expansion despite Wnt pathway hyperactivation.** (A) β-catenin immunostaining  
720 (brown) counterstained with hematoxylin (blue) on intestinal epithelium sections from  
721 Control, *Apc*<sup>cKO</sup> and *Apc*<sup>cKO</sup>; *Nle*<sup>cKO</sup> intestines at day 2 pi. The second lane shows magnified  
722 views of framed regions. Scale bars, 50 µm. (B) RT-qPCR performed on total RNA from  
723 Control, *Nle*<sup>cKO</sup>, *Apc*<sup>cKO</sup> and *Apc*<sup>cKO</sup>; *Nle*<sup>cKO</sup> intestinal epithelium extracts at day 2 pi. Graphs  
724 represent the mean fold changes ± S.E.M. for Wnt transcriptional target genes *c-Myc* and  
725 *Axin2*. n ≥ 3 for each genotype. \*, p<0.05 \*\*, p<0.01 \*\*\*, p<0.001 according to Student's t-  
726 test. (C) BrdU immunostaining (brown) counterstained with hematoxylin (blue) on  
727 intestinal epithelium sections from Control, *Apc*<sup>cKO</sup> and *Apc*<sup>cKO</sup>; *Nle*<sup>cKO</sup> intestines at day 2  
728 pi harvested 2 hours after BrdU injection. Black bars indicate the extension of the  
729 proliferative compartment. Scale bars, 50 µm. (D) Histogram showing the mean  
730 proportion (± S.E.M.) of BrdU-positive cells in the proliferative compartment in Control,  
731 *Apc*<sup>cKO</sup> and *Apc*<sup>cKO</sup>; *Nle*<sup>cKO</sup> small intestines. Twenty-five transverse crypt sections were  
732 scored per mouse, n = 4 for each genotype. The means were not significantly different  
733 among genotypes according to Mann-Whitney Wilcoxon test.

734

735 **Figure 3 Nle loss-of-function restores cell cycle exit and differentiation in the Apc-**  
736 **deficient epithelium.** (A) BrdU immunostaining (brown) counterstained with  
737 Hematoxylin (blue) on intestinal epithelium sections from Control, Apc<sup>cKO</sup> and  
738 Apc<sup>cKO</sup>; Nle<sup>cKO</sup> intestines at day 3 pi harvested 2 hours or 48 hours after BrdU injection.  
739 Plain black bars indicate the proliferative compartment. Dotted black bars indicate the  
740 range of proliferative cell migration within 48 hours. Scale bars, 50 µm. (B) Cleaved-  
741 Caspase 3 immunostaining (brown) counterstained with Hematoxylin (blue) on intestinal  
742 epithelium sections from Control, Apc<sup>cKO</sup> and Apc<sup>cKO</sup>; Nle<sup>cKO</sup> intestines at day 2 pi.  
743 Arrowheads indicate Caspase 3-positive cells. Scale bars, 50 µm. (C) MUC2  
744 immunostaining (brown) counterstained with Hematoxylin (blue) on intestinal  
745 epithelium sections from Control, Apc<sup>cKO</sup> and Apc<sup>cKO</sup>; Nle<sup>cKO</sup> intestines at day 2 pi. Scale  
746 bars, 50 µm. (D) Chromogranin A immunostaining (brown) counterstained with  
747 Hematoxylin (blue) on intestinal epithelium sections from Control, Apc<sup>cKO</sup> and  
748 Apc<sup>cKO</sup>; Nle<sup>cKO</sup> intestines at day 2 pi. Scale bars, 50 µm. (E) Histogram showing the mean  
749 number (+/-SEM) of Caspase 3 positive cells per crypt in Control, Apc<sup>cKO</sup> and  
750 Apc<sup>cKO</sup>; Nle<sup>cKO</sup> intestines at day 2 pi. 30 transverse crypts were scored per mouse, n≥3 for  
751 each genotype. \*, P<0.05 Mann-Whitney Wilcoxon test. (F) RT-qPCR performed on total  
752 RNA from Control, Apc<sup>cKO</sup> and Apc<sup>cKO</sup>; Nle<sup>cKO</sup> intestinal crypt extracts at day 2 pi. Graphs  
753 represent the mean fold changes ± S.E.M. for differentiation markers *Mucin 2* (*Muc2*) and  
754 *Chromogranin A* (*ChromoA*). n ≥ 3 for each genotype. \*, p<0.05 \*\*, p<0.01 according to  
755 Mann-Whitney Wilcoxon test.

756

757 **Figure 4 Nle loss-of-function leads to ribosome biogenesis defects and p53**  
758 **stabilization in the Apc-deficient epithelium.** (A) Simplified diagram illustrating the  
759 main steps of ribosome biogenesis in eukaryotic cells. Blue arrows represent the primers  
760 used to measure the levels of ribosomal RNAs by RT-qPCR. FISH probes used to detect  
761 its1 (red) and its2 (green) sequences from precursors of the small and large ribosomal  
762 subunits, respectively, are indicated. (B) RT-qPCR performed on total RNA from Control,  
763 Apc<sup>cKO</sup> and Apc<sup>cKO</sup>; Nle<sup>cKO</sup> intestinal crypt extracts at day 2 pi. Graphs represent the mean  
764 fold changes ± S.E.M. for the different amplicons. n = 4 for each genotype. \*, p<0.05 \*\*,  
765 p<0.01 \*\*\*, p<0.001 according to Student's t-test. (C) FISH for its1 (red) or its2 (yellow)  
766 counterstained with Hoechst (blue) on intestinal epithelium sections from Control, Apc<sup>cKO</sup>  
767 and Apc<sup>cKO</sup>; Nle<sup>cKO</sup> intestines. Scale bars, 50 µm. (D) p53 immunostaining (brown)

768 counterstained with Hematoxylin (blue) on intestinal epithelium sections from Control,  
769 Apc<sup>cKO</sup> and Apc<sup>cKO</sup>; Nle<sup>cKO</sup> intestines at day 2 pi. Lateral bars indicate the position of the  
770 crypt domain for Control and Apc<sup>cKO</sup>; Nle<sup>cKO</sup> and of the enlarged crypt-like compartment  
771 for Apc<sup>cKO</sup>. Scale bars, 50 µm.

772

773 **Figure 5 The double mutant transcriptome is the sum of simple mutant**  
774 **transcriptomes.** (A) Principal Component Analysis (PCA) of the samples. PC2 is plotted  
775 against PC1. Apc<sup>cKO</sup> (A) and Apc<sup>cKO</sup>; Nle<sup>cKO</sup> (AN) are distinguishable from Control (C) and  
776 Nle<sup>cKO</sup> (N) according to PC1, whereas N and AN are distinguishable from C and A according  
777 to PC1, meaning that PC1 corresponds to *Apc* loss-of-function and PC2 corresponds to *Nle*  
778 loss-of-function. (B) K-means clustering on all genes normalized by their maximum  
779 expression among the samples. (C) List and description of the 8 theoretical categories of  
780 genes according to the model-based analysis. -: no change; N: change in all Nle<sup>cKO</sup> samples  
781 including double mutant ones; A: change in all Apc<sup>cKO</sup> samples including double mutant  
782 ones; and D: change in double mutant Apc<sup>cKO</sup>; Nle<sup>cKO</sup> different from that predicted by the  
783 additive combination of N and A. (D) Histogram showing the distribution of genes among  
784 the 8 categories at day 1 pi and day 2 pi. The number of genes assigned to each category  
785 is indicated at both timings. (E) Genes in the [A|N|-] and [A|N|D] categories were  
786 separated into clusters by the direction of the A, N and D fold changes at day 2 pi. Gene  
787 number is plotted on the left of each heatmap. For each cluster, genes relevant to the  
788 analyzed phenotypes are indicated, as well as the most significantly enriched gene (black)  
789 and phenotype (blue) ontology terms from MouseMine. (F) Histograms showing the  
790 expression variation at day 2 pi of some cell cycle inhibitor-coding mRNAs (blue), p53  
791 transcriptional targets (red), Wnt transcriptional targets (purple) and transcripts  
792 enriched in ISCs (red). ns, fold change not significant.

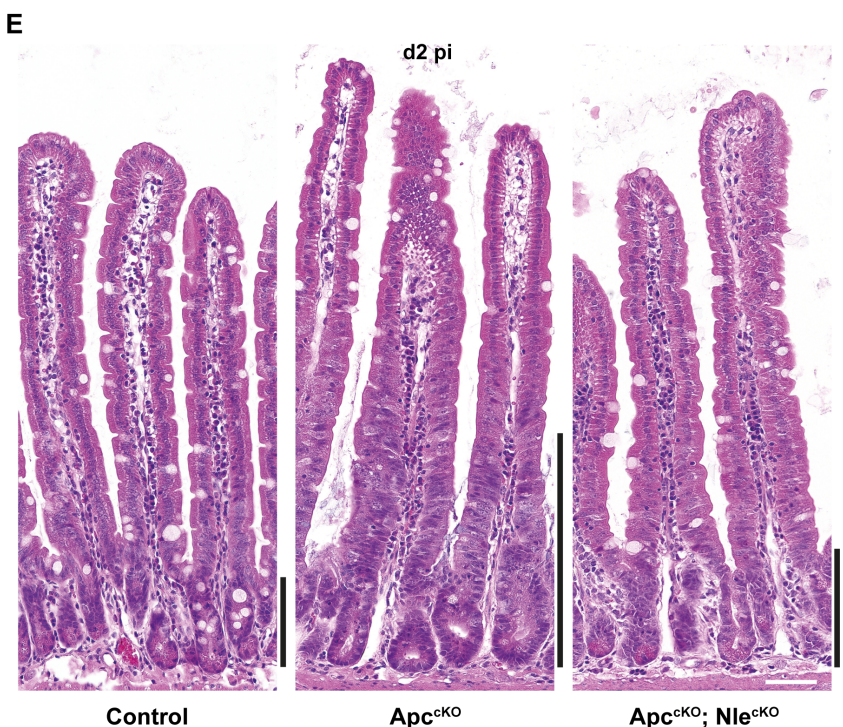
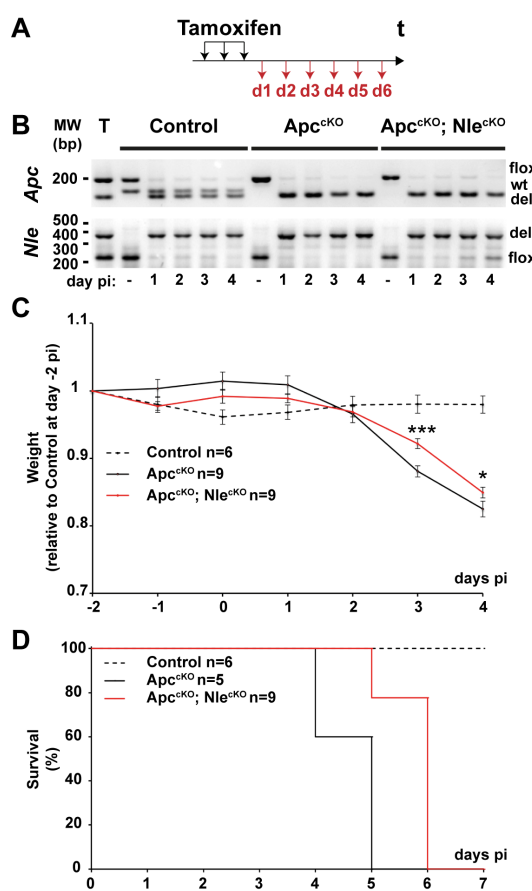
793

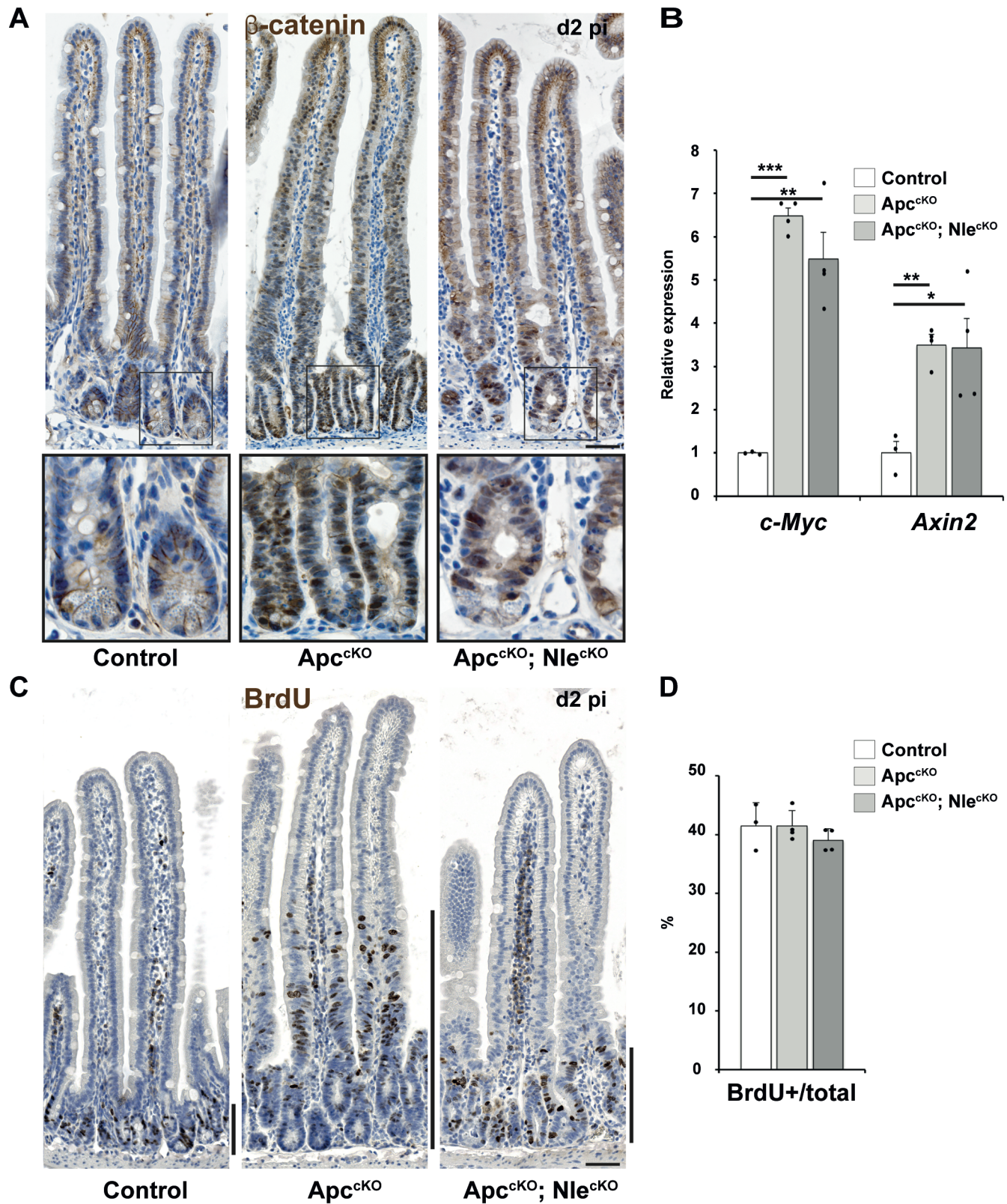
794 **Figure 6 Nle loss-of-function causes a diminution of mature rRNA levels and global**  
795 **protein synthesis in the *Apc*-deficient epithelium.** (A) RT-qPCR for 18S and 28S rRNA  
796 performed on total RNA from Control, Apc<sup>cKO</sup> and Apc<sup>cKO</sup>; Nle<sup>cKO</sup> intestinal crypt extracts  
797 at day 2 pi. Graphs represent the mean fold changes ± S.E.M. for the different amplicons.  
798 n = 4 for each genotype. \*, p<0.05 \*\*, p<0.01 according to Student's t-test. (B) Anti-  
799 puromycin immunoblotting of protein extracts for identical number of crypts cells from  
800 Control, Apc<sup>cKO</sup> and Apc<sup>cKO</sup>; Nle<sup>cKO</sup> intestines at day 2 pi. (C) Histogram showing the mean

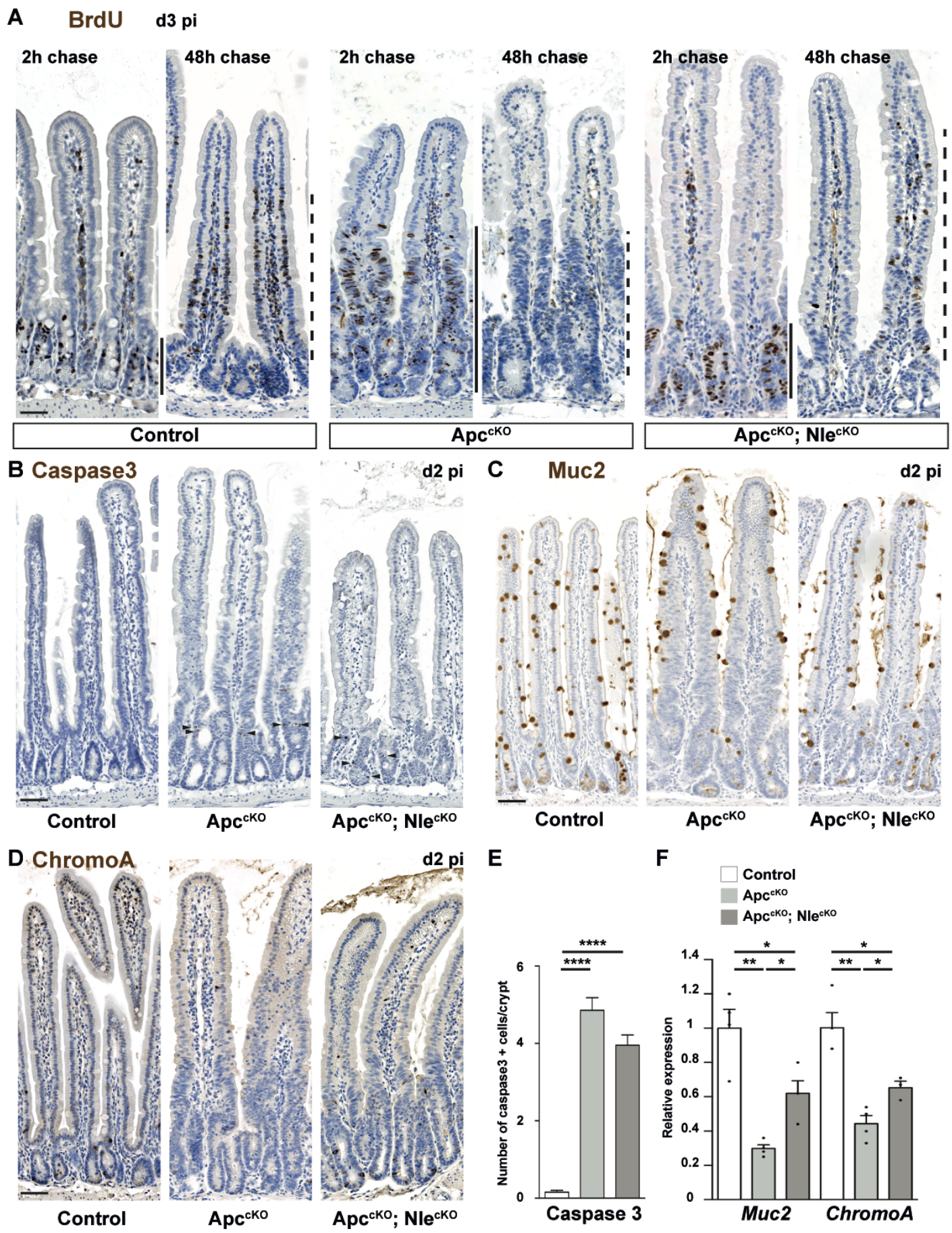
801 normalized signal intensity  $\pm$  S.E.M from the immunoblot shown in (B). n = 4 for each  
802 genotype. \*, p<0.05 according to Mann–Whitney Wilcoxon test.

803  
804 **Figure 7 Apc loss-of-function attenuates stem cell loss following Nle deletion.** (A) RT-  
805 qPCR performed on total RNA from Control, Nle<sup>cKO</sup>, Apc<sup>cKO</sup> and Apc<sup>cKO</sup>; Nle<sup>cKO</sup> intestinal  
806 crypt extracts at day 2 pi. Graphs represent the mean fold changes  $\pm$  S.E.M. for ISC markers  
807 Lgr5 and Olfm4. n = 4 for each genotype. \*, p<0.05 \*\*, p<0.01 \*\*\*, p<0.001 according to  
808 Student's t-test. (B) In situ hybridization for Olfm4 mRNA (brown) counterstained with  
809 Hematoxylin (blue) on intestinal epithelium sections from Control, Nle<sup>cKO</sup>, Apc<sup>cKO</sup> and  
810 Apc<sup>cKO</sup>; Nle<sup>cKO</sup> intestines. The second lane shows magnified views of framed regions. Scale  
811 bars, 50  $\mu$ m. (C) p53 immunostaining (brown) counterstained with Hematoxylin (blue)  
812 on crypt sections from Apc<sup>cKO</sup>; Nle<sup>cKO</sup> intestines at days 2, 3 and 4 pi. Asterisks indicate  
813 p53-positive CBCs. Scale bars, 25  $\mu$ m. (D) BrdU immunostaining (brown) counterstained  
814 with Hematoxylin (blue) on crypt sections from Control, Nle<sup>cKO</sup>, Apc<sup>cKO</sup> and Apc<sup>cKO</sup>; Nle<sup>cKO</sup>  
815 intestines at day 2 pi harvested 2 hours after BrdU injection. Asterisks indicate BrdU-  
816 positive CBCs. Scale bars, 25  $\mu$ m.

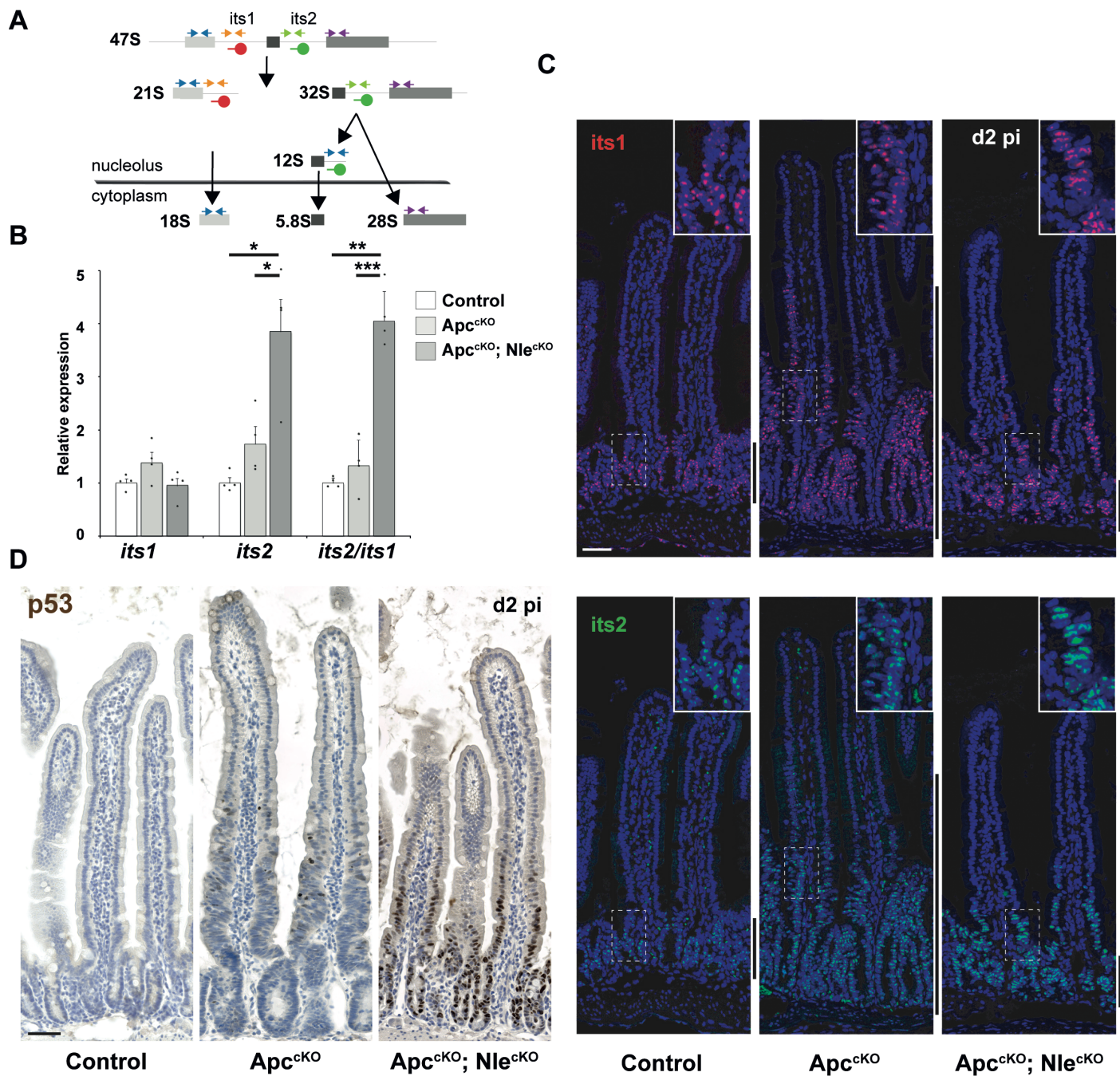
817  
818 **Figure 8 Apc<sup>cKO</sup> intestinal organoids show increased tolerance to Nle-deficiency and**  
819 **p53 stabilization.** (A) Histogram showing the mean percentage ( $\pm$  S.E.M.) of organoid  
820 formation and survival at day 4 pi from an initial culture of 400 crypts per well from  
821 Control, Nle<sup>cKO</sup>, Apc<sup>cKO</sup> and Apc<sup>cKO</sup>; Nle<sup>cKO</sup> intestines harvested at day 1 pi. n  $\geq$  3  
822 experiments for each genotype. (B) Pictures of organoids obtained from Control, Nle<sup>cKO</sup>,  
823 Apc<sup>cKO</sup> and Apc<sup>cKO</sup>; Nle<sup>cKO</sup> crypts. The top lane shows a global view of a well for each  
824 genotype at day 4 pi. The middle lane (resp. bottom lane) shows the morphology of  
825 organoids of the different genotypes at day 4 (resp. 6) pi. (C) Histogram showing the mean  
826 percentage ( $\pm$  S.E.M.) of healthy organoids after 48h culture with various concentration  
827 of nutlin-3. (D) Pictures of Control and Apc<sup>cKO</sup> organoids after 48h in mock and 10 $\mu$ M  
828 nutlin-3 culture conditions. Under nutlin-3 treatment, many Control organoids displayed  
829 abnormal morphology (star) with absence of budding, swelling and increased opacity  
830 likely resulting from increased accumulation of dead cells in the lumen while some Apc<sup>cKO</sup>  
831 spheroids were of irregular shape, opaque and collapsed (arrowhead). Such unhealthy  
832 structures were usually degenerating in the following days of culture. \*, p<0.05 \*\*, p<0.01  
833 according to Mann-Whitney Wilcoxon test. Scale bars, 150  $\mu$ m.

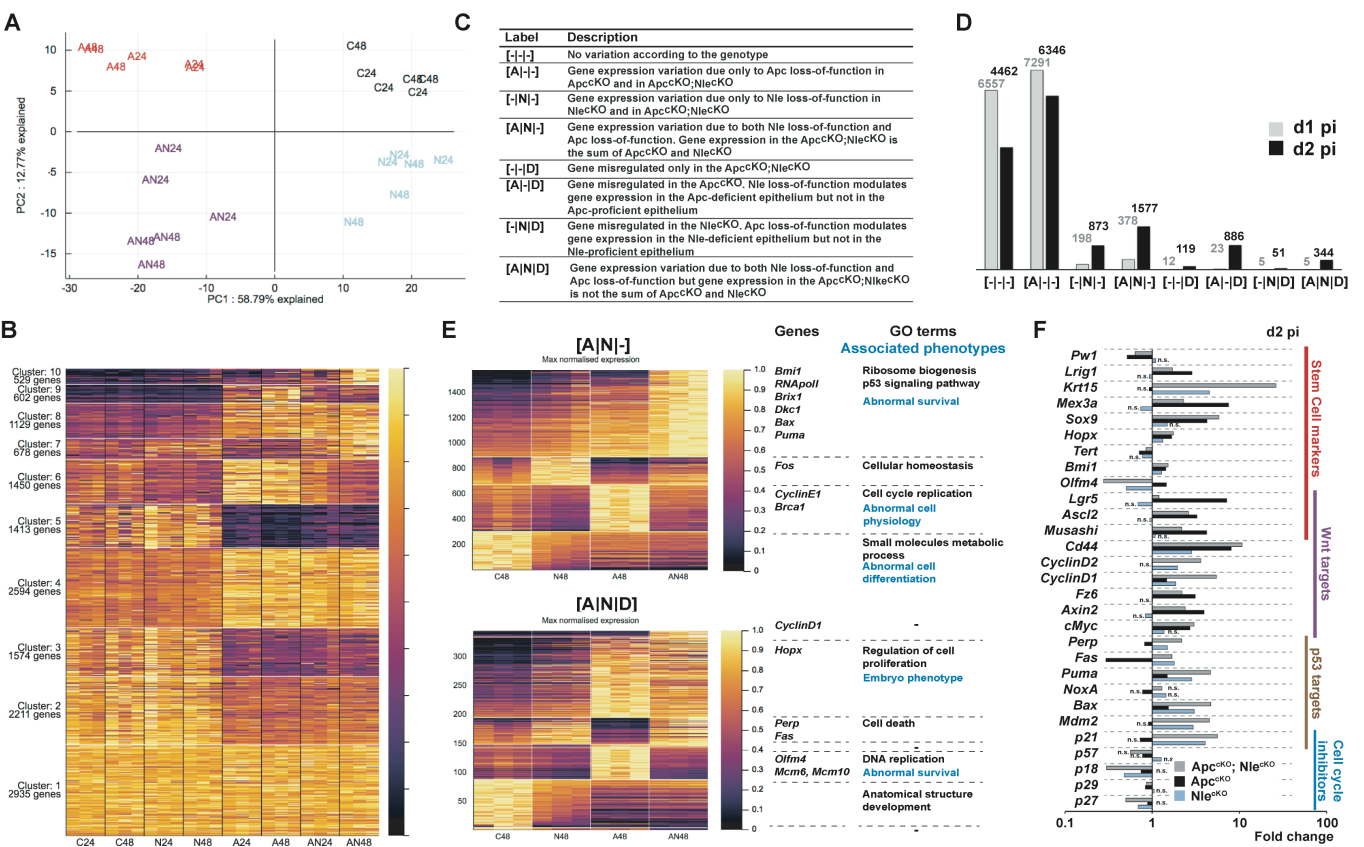


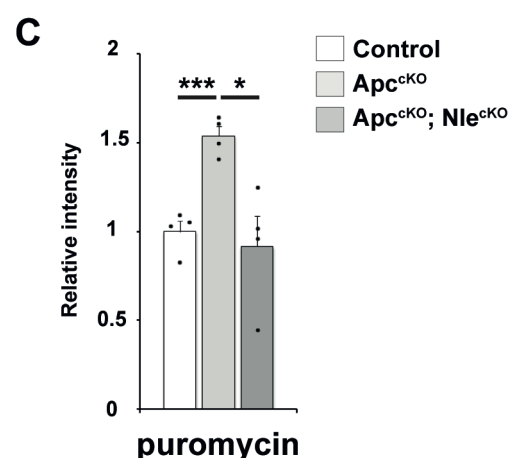
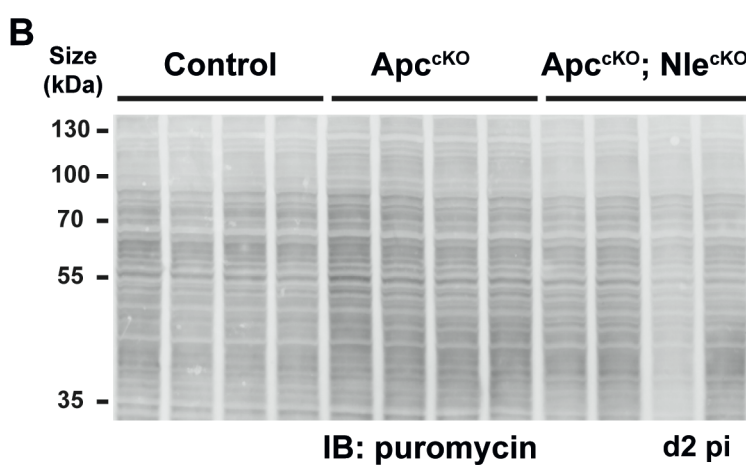
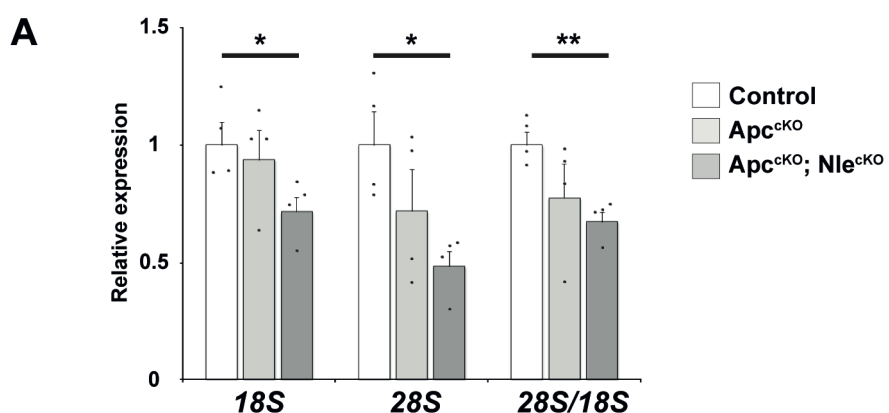


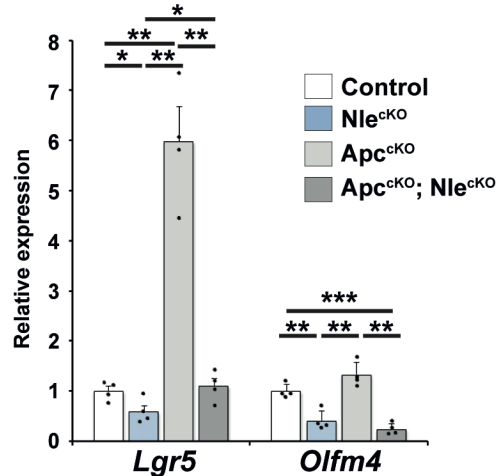
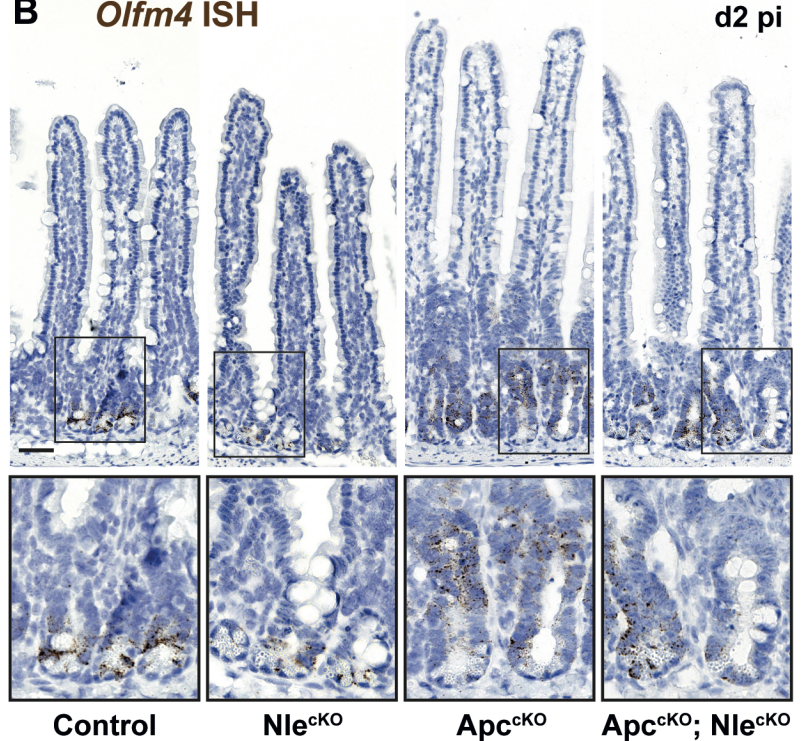
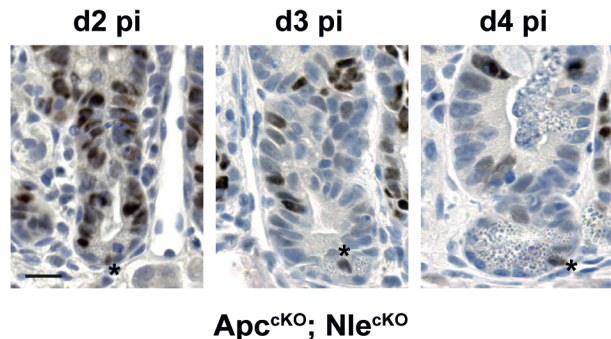


**Figure 3**

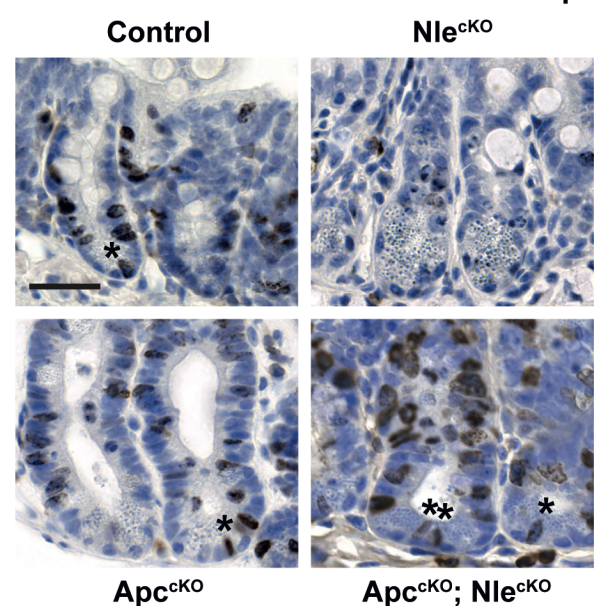


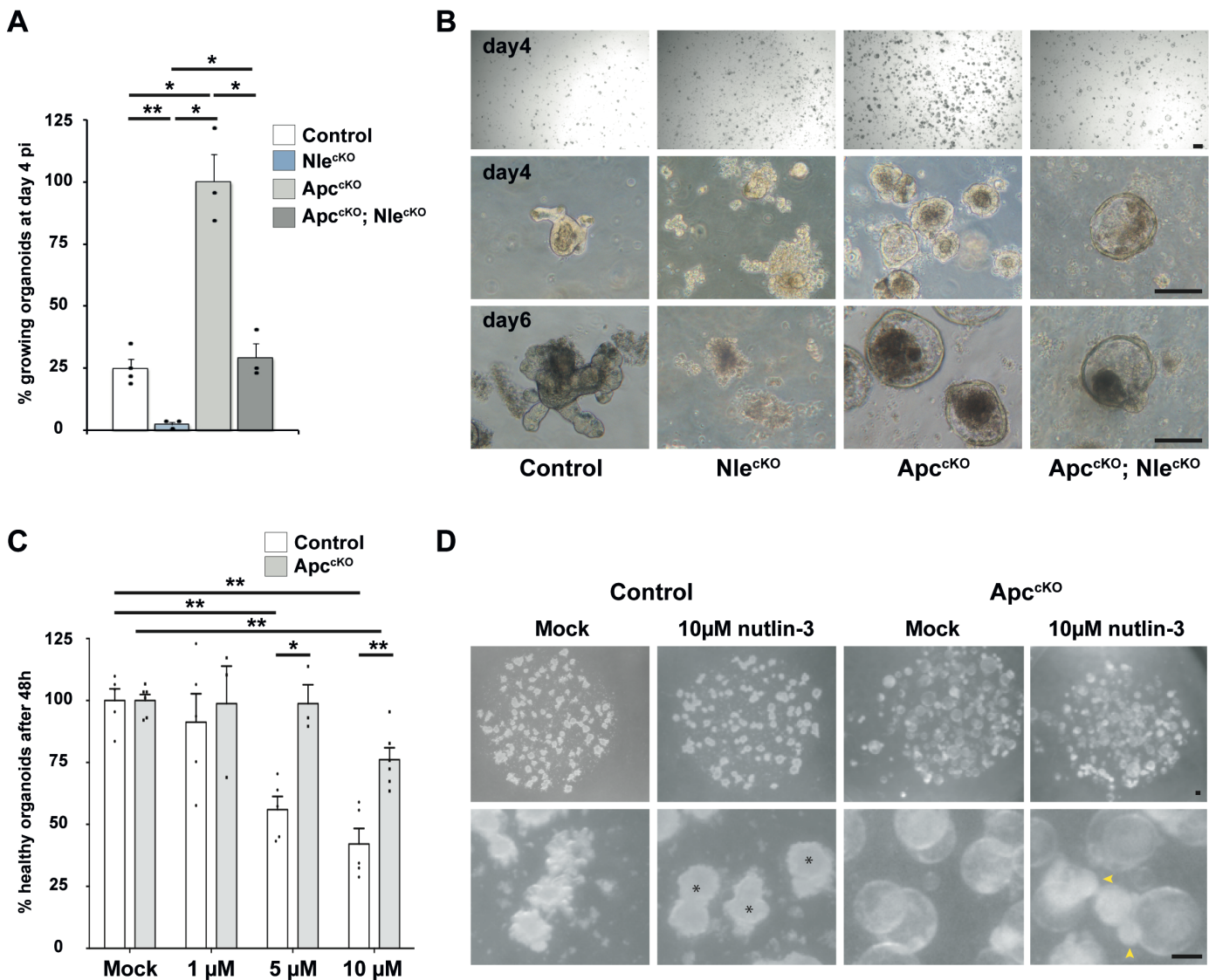




**A****B** *Olfm4* ISH**C** p53**D**

BrdU 2h chase





## **Supplementary Figures**

### **Compensation between Wnt-driven tumorigenesis and cellular responses to ribosome biogenesis inhibition in the murine intestinal epithelium**

Aurélien Raveux, Aline Stedman, Sabrina Coqueran, Sandrine Vandormael-Pournin, Nick Owens, Béatrice Romagnolo and Michel Cohen-Tannoudji

This file contains 7 supplementary figures and 2 supplementary tables :

**Figure S1 : *Nle* loss-of-function only partially restores epithelial histology in the *Apc*-deficient intestine.**

**Figure S2: *Nle* loss-of-function reduces proliferative compartment expansion rate in the *Apc*-deficient epithelium.**

**Figure S3: Cell cycle exit is delayed in the double mutant compared to the control.**

**Figure S4: *Nle* loss-of-function induces persistent p53 stabilization in the *Apc*-deficient epithelium.**

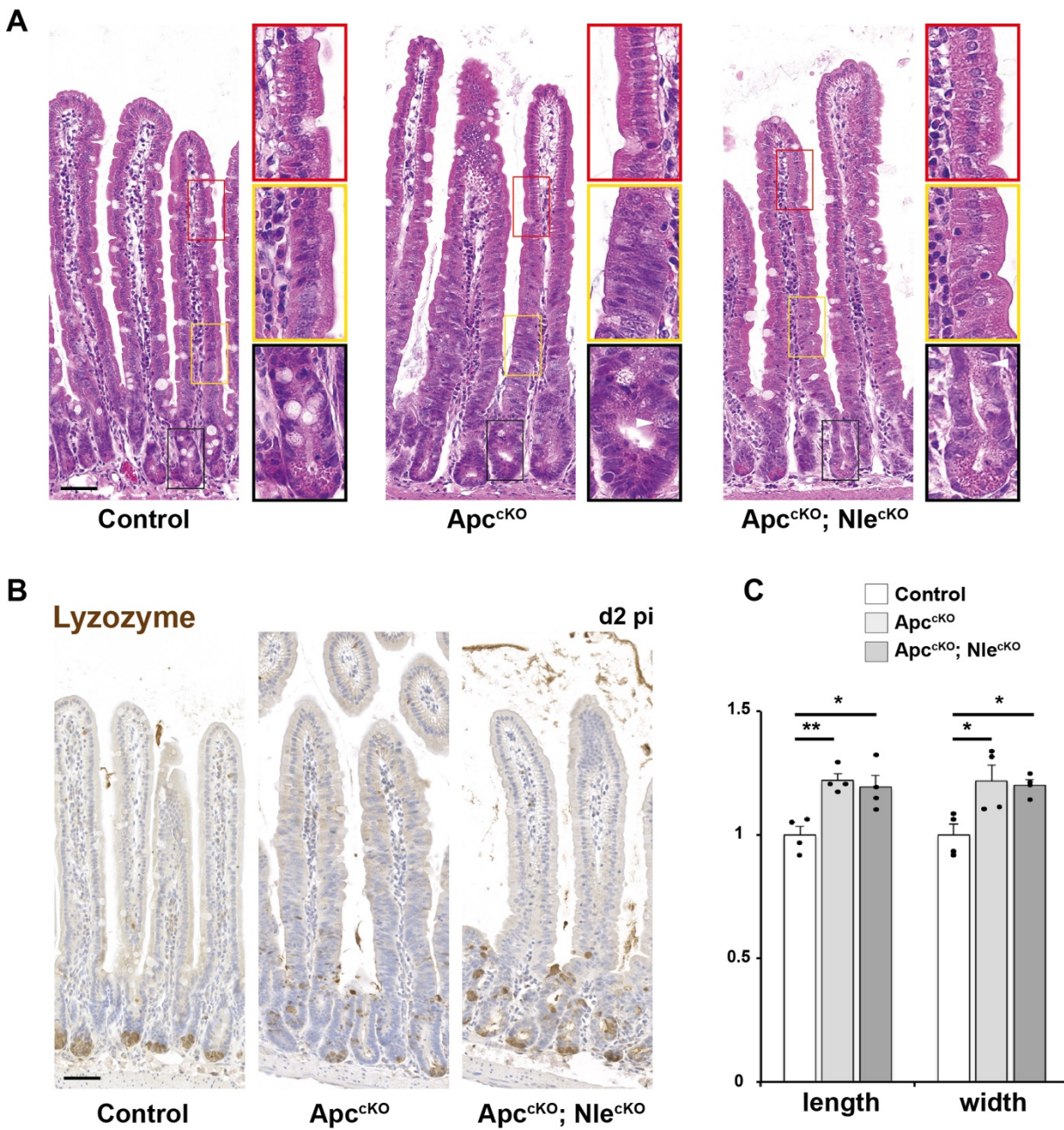
**Figure S5: Functional analysis of gene clusters does not indicate signaling pathway interference between *Apc* loss-of-function and *Nle* loss-of-function.**

**Figure S6: Global protein synthesis at day 3 pi**

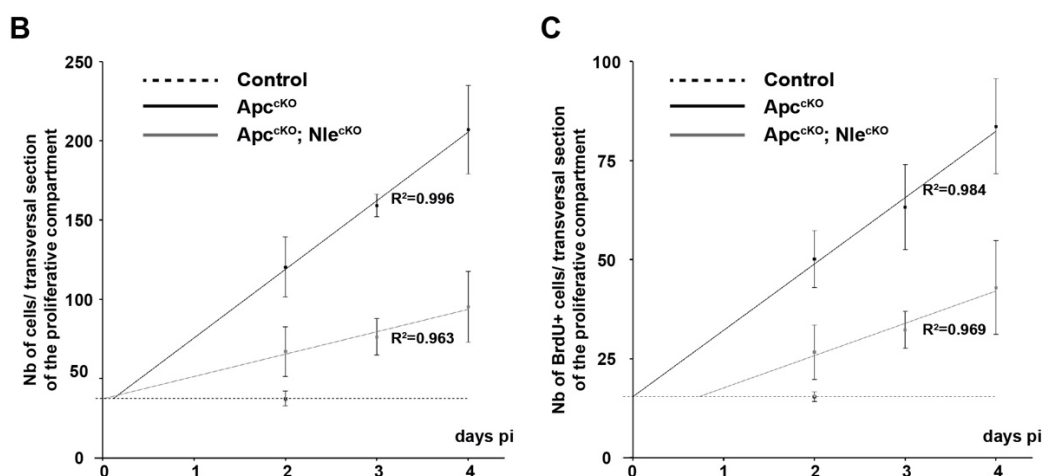
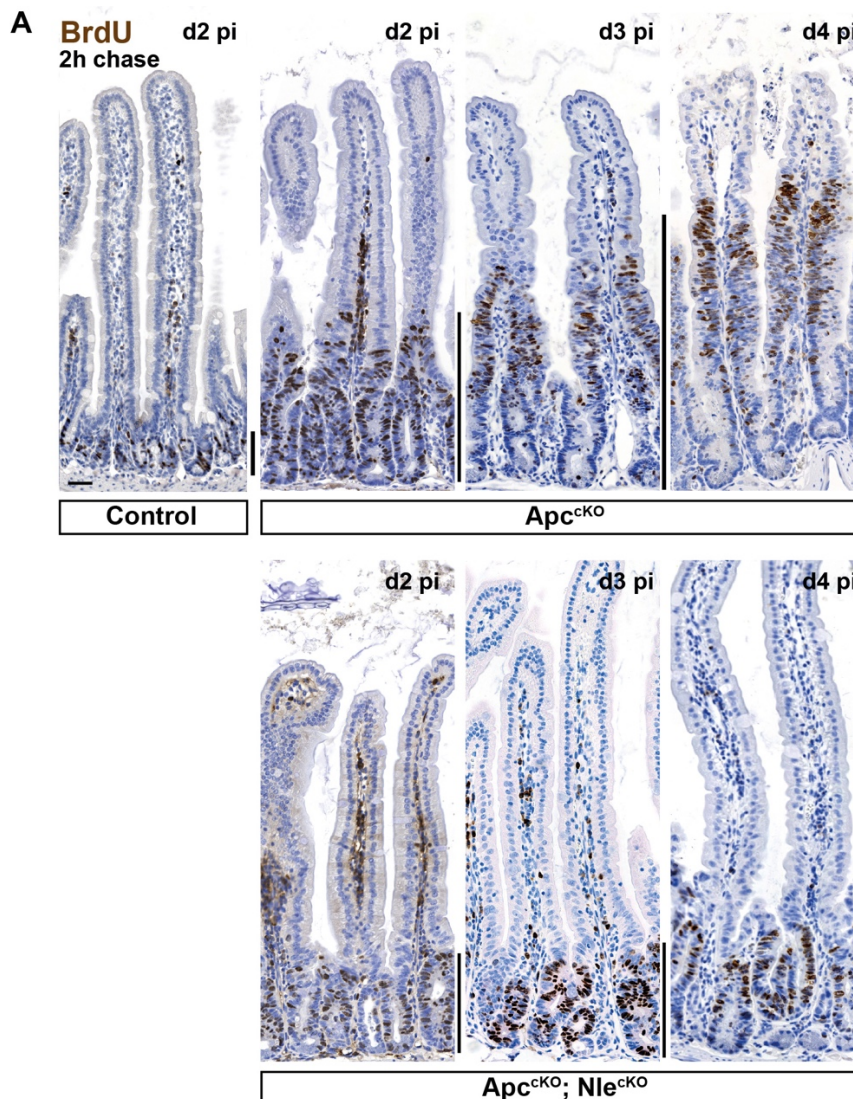
**Figure S7: Derivation and nutlin-3 treatment of intestinal organoids**

**Supplementary Table 1: list of primary and secondary antibodies**

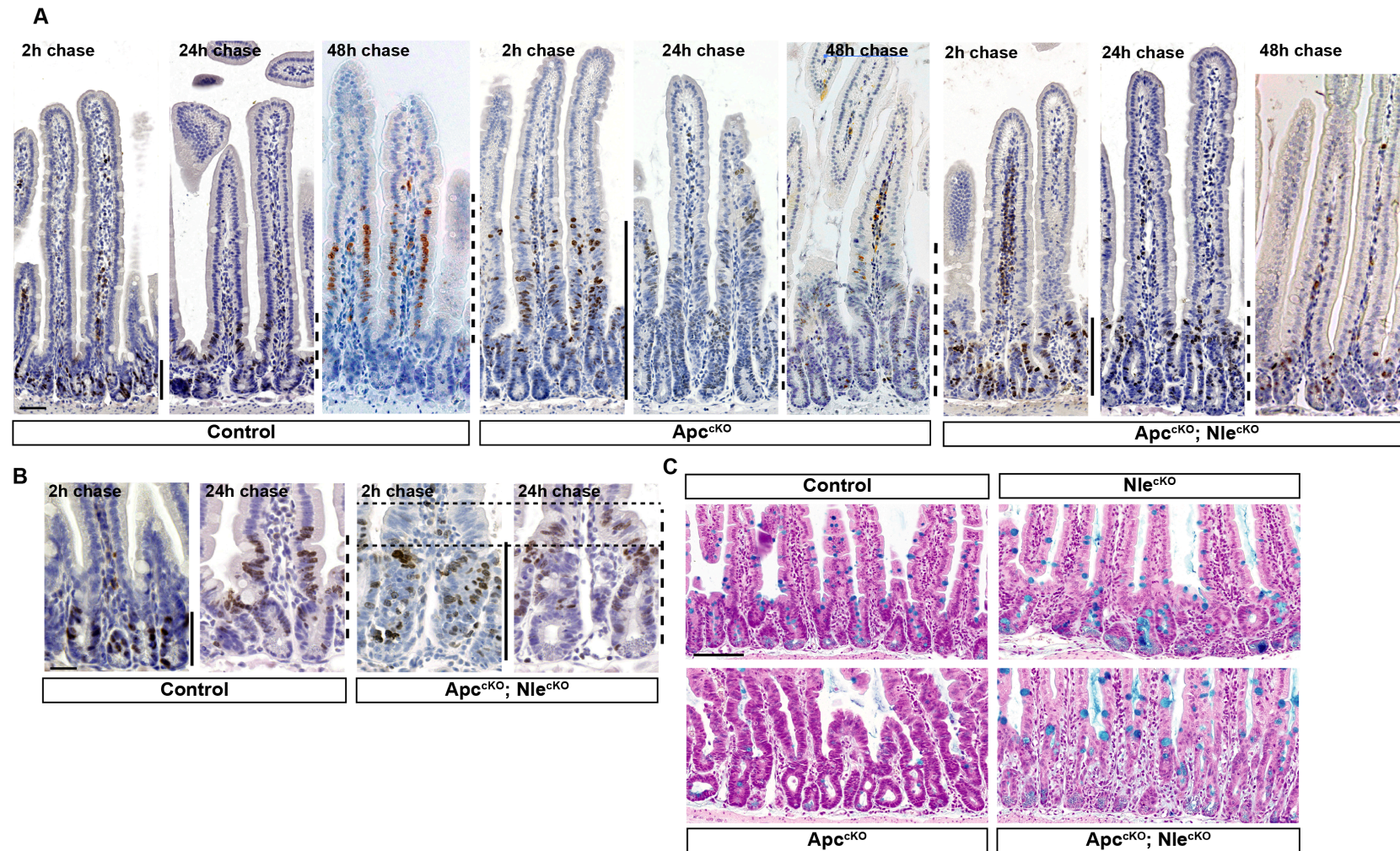
**Supplementary Table 2: Sequences of RT-qPCR primers**



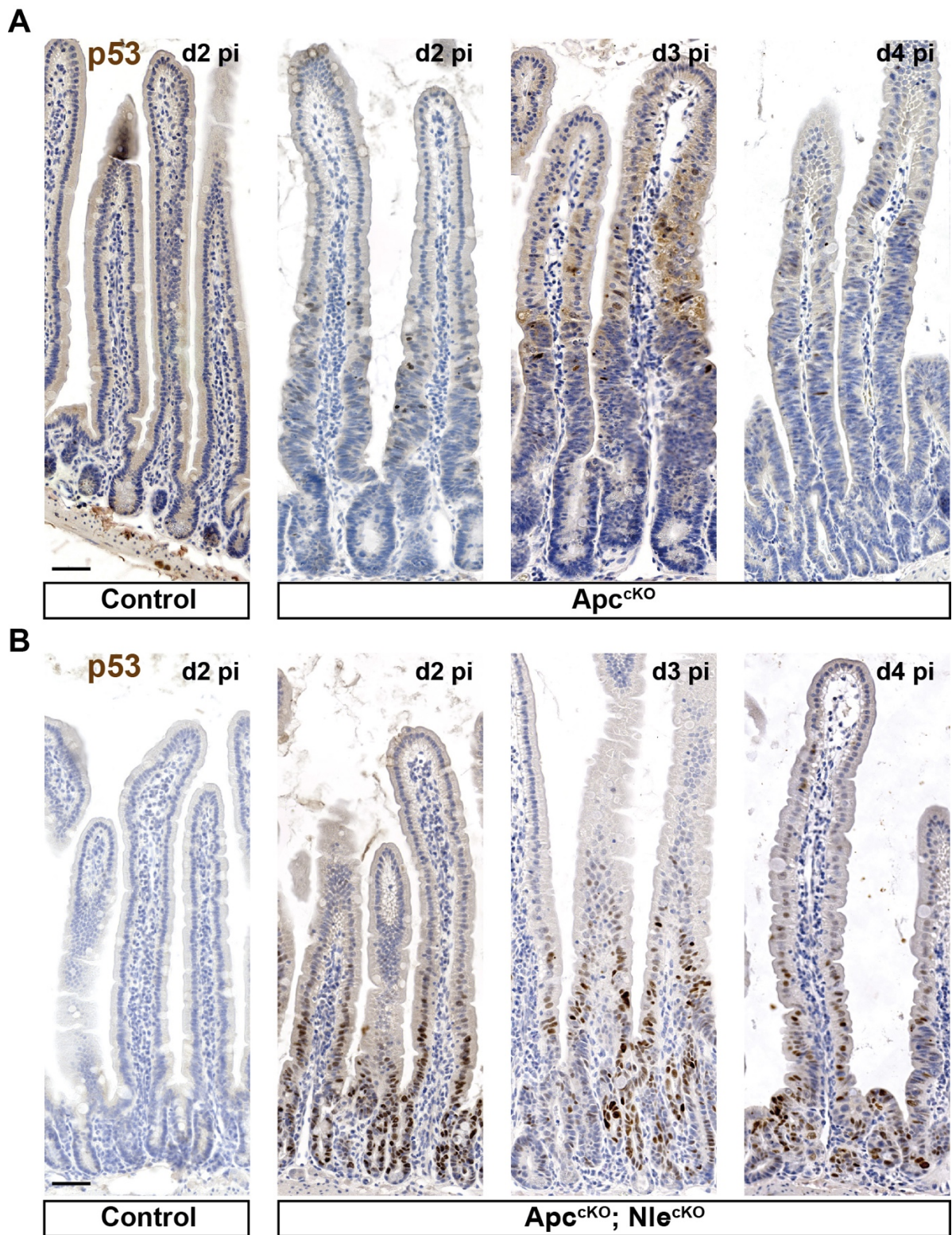
**Figure S1 Nle loss-of-function only partially restores epithelial histology in the *Apc*-deficient intestine.** (A) Hematoxylin-eosin staining of intestinal epithelium sections from Control,  $\text{Apc}^{\text{cKO}}$  and  $\text{Apc}^{\text{cKO}};\text{Nle}^{\text{cKO}}$  small intestines at day 2 pi. Scale bars, 50  $\mu\text{m}$ . For each genotype, a portion of the villus is magnified (top) to highlight enterocyte hypertrophy, as well as a portion of the enlarged crypt compartment in the  $\text{Apc}^{\text{cKO}}$  and of the corresponding villus section in the other genotypes (middle) to highlight epithelial architecture restoration in the  $\text{Apc}^{\text{cKO}};\text{Nle}^{\text{cKO}}$ , and a magnification of the histological crypt (bottom) is shown to highlight the presence of cells with granules (arrowheads) in the  $\text{Apc}^{\text{cKO}}$  and  $\text{Apc}^{\text{cKO}};\text{Nle}^{\text{cKO}}$ . (B) Lysozyme immunostaining (brown) counterstained with Hematoxylin (blue) on intestinal epithelium sections from Control,  $\text{Apc}^{\text{cKO}}$  and  $\text{Apc}^{\text{cKO}};\text{Nle}^{\text{cKO}}$  intestines at day 2 pi. Scale bars, 50  $\mu\text{m}$ . (C) Histogram showing the mean ( $\pm$  S.E.M.) length (defined as the lateral membrane section length) and width (defined as the apical or basal membrane section length) of enterocytes in Control,  $\text{Apc}^{\text{cKO}}$  and  $\text{Apc}^{\text{cKO}};\text{Nle}^{\text{cKO}}$  villi. Twenty-five transverse sections of enterocytes homogeneously distributed along the jejunum were scored per mouse,  $n = 4$  mice for each genotype. Means were normalized according to mean control measurements. \*,  $p < 0.05$  \*\*,  $p < 0.01$  according to Student's t-test. Differences that were significant according to Student's t-test were also significant according to Mann-Whitney Wilcoxon test with  $p < 0.05$ .



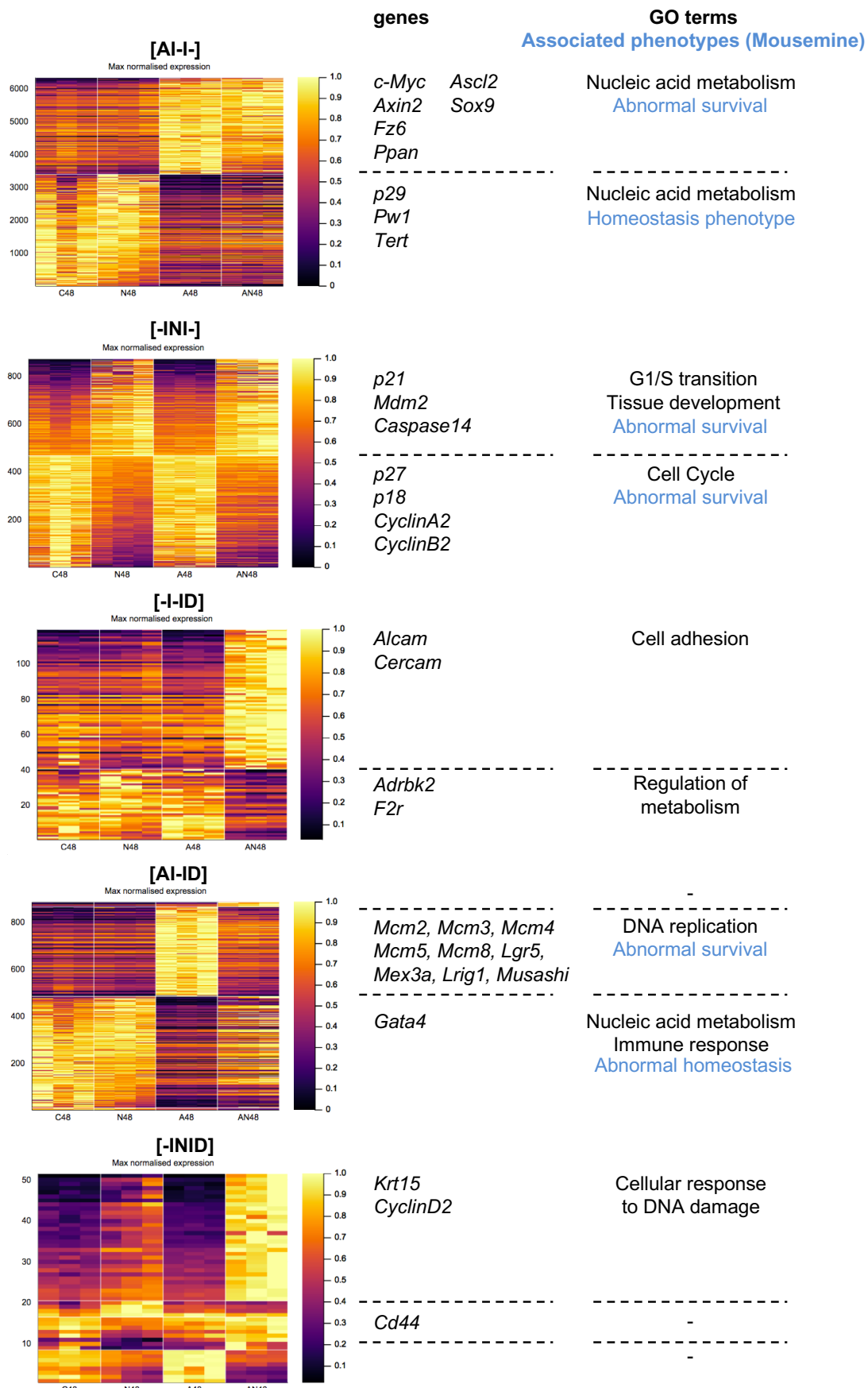
**Figure S2 Nle loss-of-function reduces proliferative compartment expansion rate in the *Apc*-deficient epithelium.** (A) BrdU immunostaining (brown) counterstained with hematoxylin (blue) on intestinal epithelium sections from Control (day 2 pi), Apc<sup>cKO</sup> and Apc<sup>cKO</sup>; Nle<sup>cKO</sup> (days 2, 3 and 4 pi) intestines harvested 2 hours after BrdU injection. Scale bars, 50  $\mu$ m. (B-C) Graphs showing the mean total cell number (B) and the mean number of BrdU-positive-cells (C) in a transverse section of the proliferative compartment of Control, Apc<sup>cKO</sup> and Apc<sup>cKO</sup>; Nle<sup>cKO</sup> intestines at several timing post tamoxifen injection. Twenty-five transverse crypt sections were scored per mouse,  $n = 4$  for each genotype and each time point.  $R^2$ , correlation coefficient with a linear model (plain regression lines). The dotted horizontal line shows baseline Control levels according to day 2 pi measurements. Hypothesizing linear growth, proliferative compartment expansion begins at 0 day pi in the Apc<sup>cKO</sup> as previously reported [10] and in the Apc<sup>cKO</sup>; Nle<sup>cKO</sup>.



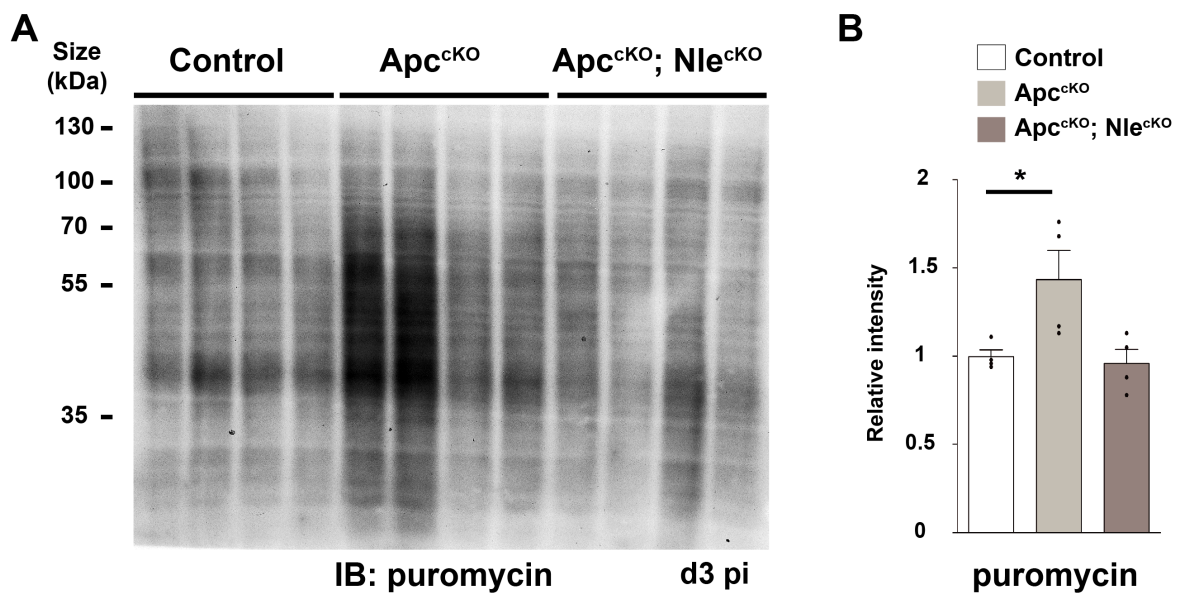
**Figure S3 Cell cycle exit is delayed in the double mutant compared to the control.** (A) BrdU immunostaining (brown) counterstained with Hematoxylin (blue) on intestinal epithelium sections from Control and *Apc<sup>cKO</sup>; Nle<sup>cKO</sup>* intestines at day 2 pi harvested 2, 24 or 48 hours after BrdU injection. Plain black bars indicate the proliferative compartment. Dotted black bars indicate the range of proliferative cell migration within 24 or 48 hours. Scale bars, 50  $\mu$ m. (B) BrdU immunostaining (brown) counterstained with Hematoxylin (blue) on crypt sections from Control and *Apc<sup>cKO</sup>; Nle<sup>cKO</sup>* intestines at day 2 pi harvested 2 hours or 24 hours after BrdU injection. Plain black bars indicate the proliferative compartment. The dotted horizontal lines indicate the limits of the double-mutant specific compartment (see text). Scale bars, 25  $\mu$ m. (C) Alcian blue coloration counterstained with Nuclear Fast Red on intestinal epithelium sections from Control, *Nle<sup>cKO</sup>*, *Apc<sup>cKO</sup>* and *Apc<sup>cKO</sup>; Nle<sup>cKO</sup>* intestines at day 3 pi. Scale bars, 100  $\mu$ m.



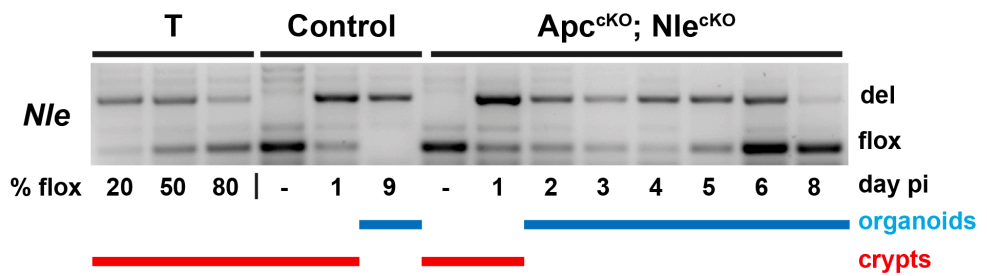
**Figure S4 Nle loss-of-function induces persistent p53 stabilization in the *Apc*-deficient epithelium.** (A) p53 immunostaining (brown) counterstained with Hematoxylin (blue) on intestinal epithelium sections from Control (day 2 pi) and *Apc*<sup>cKO</sup> (days 2, 3 and 4 pi) intestines. Scale bars, 50 µm. (B) p53 immunostaining (brown) counterstained with Hematoxylin (blue) on intestinal epithelium sections from Control (day 2 pi) and *Apc*<sup>cKO</sup>; *Nle*<sup>cKO</sup> (days 2, 3 and 4 pi) intestines. Scale bars, 50 µm.



**Figure S5 Functional analysis of gene clusters does not indicate signaling pathway interference between *Apc* loss-of-function and *Nle* loss-of-function.** Genes in the [A|N|-] and [A|N|D] categories were separated into clusters by the direction of the A, N and D fold changes at day 2 pi. Gene number is plotted on the left of each heatmap. For each cluster, genes relevant to the analyzed phenotypes are indicated, as well as the most significantly enriched gene (black) and phenotype (blue) ontology terms from MouseMine.



**Figure S6 Global protein synthesis at day 3 pi.** (A) Anti-puromycin immunoblotting of protein extracts for identical number of crypts cells from Control,  $Apc^{cKO}$  and  $Apc^{cKO}; Nle^{cKO}$  intestines at day 3 pi. (B) Histogram showing the mean normalized signal intensity  $\pm$  S.E.M from the immunoblot shown in (A). n = 4 for each genotype. \*, p<0.05 according to Mann–Whitney Wilcoxon test.

**A****B**

$Apc^{cKO}$  organoid 5 $\mu$ M nutlin-3 for 48h

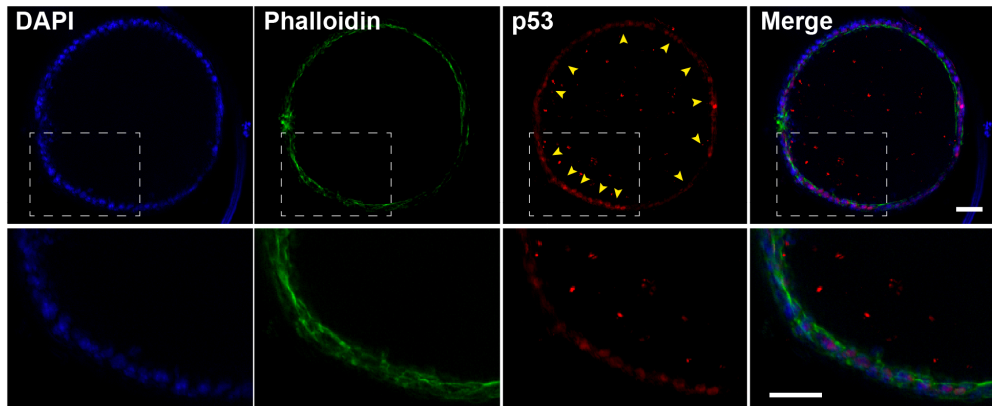


**Figure S7 Derivation and nutlin-3 treatment of intestinal organoids** (A) Detection of the nonrecombined (flox) and the recombined (del) *Nle* alleles by PCR performed on DNA extracts from Control and  $Apc; Nle^{VilcKO}$  wells at different time points. Control DNAs with 20%, 50% and 80% flox alleles obtained by mixing  $Nle^{flox/+}$  and  $Nle^{flox/del}$  DNAs are presented. The  $Nle^{+}$  and  $Nle^{null}$  alleles are not shown on the gel. (A) p53 immunostaining of an  $APC^{cKO}$  organoid cultured for 48h with 5 $\mu$ M nutlin-3. A single optical section is shown. Note the presence of numerous p53 positive nuclei on the whole circumference of the spheroid. Bright dots correspond to non specific staining of debris present in the lumen of the organoid. Bar: 50 $\mu$ M.

**Supplementary Table 1: list of primary and secondary antibodies**

Antibodies	Reference	Dilution used
anti-cleaved Caspase 3	9661L Ozyme	1/200
anti-BrdU	347580 BD	1/150
anti-β-catenin	C19220 BD	1/50
anti-p53	CM5-p Leica	1/500
anti-lysozyme	A0099 Dako	1/1000
anti-Muc2	sc-15334 Santa-Cruz	1/200
anti-ChromoA	sc-1488 Santa-Cruz	1/300
anti-puromycin	5B12, David <i>et al.</i> , JCB 2012	1/5000
Biotinylated goat anti-rabbit IgG	E0432 Dako	1/400
Biotinylated goat anti-mouse IgG	E0433 Dako	1/400

**Supplementary Table 2: Sequences of RT-qPCR primers**

Target gene	Forward primer	Reverse primer
<i>Olfm4</i>	ATCAGCGCTCCTCTGTGAT	AGGGTTCTCTGGATGCTG
<i>Lgr5</i>	ACATTCCAAGGGAGCGTTC	ATGTGGTGGCATCTAGGCG
<i>Muc2</i>	CAAGGGCTCGGAACTCCAG	CCAGGGAATCGGTAGACATCG
<i>ChromoA</i>	AGTCATCTCGACTCGCTGT	GGTGTGCGAGGATAGAGAGG
<i>c-Myc</i>	AAGGCCCAAGGTAGTG	TGCTCGTCTGCTGAATGGA
<i>Axin 2</i>	GATTCCCCTTGACCAGGTGG	CCATTACAAGCAAACCAGAAAGT
<i>Its1</i>	TCTGACCTGCCACCTA	CCTCGTAGACACGGAAGAGC
<i>Its2</i>	TGTGTGTGTTGGGTCTTGC	GGATACCACCTCTCCGTT
<i>28S</i>	TCATCAGACCCAGAAAAGG	GATTGGCAGGTGAGTTGTT
<i>18S</i>	CGGCTACCACATCCAAGGAA	GCTGGAATTACCGCGGCT